573069

Far Ultraviolet Spectroscopy of the Intergalactic and Interstellar Absorption Toward 3C 273

Kenneth R. Sembach[1], J. Christopher Howk[1], Blair D. Savage[2], J. Michael Shull[3], and William R. Oegerle[4]

ABSTRACT

We present *Far Ultraviolet Spectroscopic Explorer* observations of the molecular, neutral atomic, weakly ionized, and highly ionized components of the interstellar and intergalactic material toward the quasar 3C 273. We identify Lyβ absorption in 8 of the known intergalactic Lyα absorbers along the sight line with rest-frame equivalent widths W_r(Lyα) $\gtrsim$ 50 mÅ. Refined estimates of the H I column densities and Doppler parameters (b) of the clouds are presented. We find a range of $b \approx 16 - 46$ km s^{-1}. We detect multiple H I lines (Lyβ – Lyθ) in the 1590 km s^{-1} Virgo absorber and estimate $\log N$(H I) $= 15.85\pm^{0.10}_{0.08}$, ten times more H I than all of the other absorbers along the sight line combined. The Doppler width of this absorber, $b \approx 16$ km s^{-1}, implies $T \lesssim 15,000$ K. We detect O VI absorption at 1015 km s^{-1} at the $2 - 3\sigma$ level that may be associated with hot, X-ray emitting gas in the Virgo Cluster. We detect weak C III and O VI absorption in the IGM at $z = 0.12007$; this absorber is predominantly ionized and has N(H$^+$)/N(H I) $\geq 4000\,Z^{-1}$, where Z is the metallicity.

Strong Galactic interstellar O VI is present between -100 and $+100$ km s^{-1}, with an additional high-velocity wing containing about 13% of the total O VI between $\sim +100$ and $\sim +240$ km s^{-1}. The Galactic O VI, N V, and C IV lines have similar shapes, with roughly constant ratios across the -100 to $+100$ km s^{-1} velocity range. The high velocity O VI wing is not detected in other species. Much of the interstellar high ion absorption probably occurs within a highly fragmented medium within the Loop IV remnant or in the outer cavity walls of the remnant. Multiple hot gas production mechanisms are required. The broad O VI absorption wing likely traces the expulsion of hot gas out of the Galactic disk into the halo. A flux limit of 5.4×10^{-16} erg cm^{-2} s^{-1} on the amount of diffuse O VI emission present $\sim 3.5'$ off the 3C 273 sight line combined with the observed

[1]Department of Physics and Astronomy, The Johns Hopkins University, Baltimore, MD 21218

[2]Department of Astronomy, University of Wisconsin, Madison, WI 53706

[3]CASA and JILA, Department of Astrophysical and Planetary Sciences, University of Colorado, Boulder, CO 80309

[4]Laboratory for Astronomy and Solar Physics, Code 681, Goddard Space Flight Center, Greenbelt, MD 20771

O VI column density toward 3C 273, $\log N(\text{O VI}) = 14.73 \pm 0.04$, implies $n_e \lesssim 0.02\,\text{cm}^{-3}$ and $\text{P}/k \lesssim 11{,}500\,\text{cm}^{-3}\,\text{K}$ for an assumed temperature of 3×10^5 K. The elemental abundances in the neutral and weakly-ionized interstellar clouds are similar to those found for other halo clouds. The warm neutral and warm ionized clouds along the sight line have similar dust-phase abundances, implying that the properties of the dust grains in the two types of clouds are similar. Interstellar H_2 absorption is present at positive velocities at a level of $\log N(H_2) \sim 15.71$, but is very weak at the velocities of the main column density concentration along the sight line observed in H I 21 cm emission.

Subject headings: cosmology: observations – galaxies: intergalactic medium – Galaxy: halo – ISM: abundances – ISM: molecules – quasars: absorption lines

1. Introduction

The 3C 273 sight line ($l = 289.95°$, $b = +64.36°$, $z_{QSO} = 0.1583$) is one of the best studied directions in the sky at ultraviolet wavelengths. It has been the subject of numerous spectroscopic investigations encompassing studies of the ionization, kinematics, and chemical composition of the Milky Way interstellar medium (ISM; York et al. 1984; Burks et al. 1991, 1994; Savage et al. 1993; Sembach, Savage, & Tripp 1997), the content and evolution of the intergalactic medium (IGM; Morris et al. 1991; Bahcall et al. 1991, 1993; Brandt et al. 1993, 1997; Weymann et al. 1995; Hurwitz et al. 1998; Penton, Shull, & Stocke 2000; Penton, Stocke, & Shull 2000), and the relationship of the intergalactic Lyα absorption features to galaxies (e.g., Morris et al. 1993; Penton, Stocke, & Shull 2001). The sight line contains 18 intergalactic Lyα gas clouds at redshifts $z = 0.00338 - 0.14560$. In this paper we present new *Far Ultraviolet Spectroscopic Explorer* (*FUSE*) observations of 3C 273 that expand upon the previous investigations of the ISM and IGM in this direction.

FUSE is the first far-ultraviolet ($\lambda < 1200\,\text{Å}$) observatory to have both the sensitivity and spectral resolution necessary to perform detailed investigations of the kinematics and composition of the ISM and IGM in the directions of QSOs and active galactic nuclei (AGNs). The *FUSE* bandpass contains important diagnostics of molecular, atomic, and ionized gases (see Sembach 1999). Of paramount importance is the ability of *FUSE* to detect the higher Lyman series lines of H I and ionized gas lines of C III λ977.020 and O VI $\lambda\lambda$1031.926, 1037.617 in the Milky Way ISM and low-redshift universe. *FUSE* investigations of intergalactic absorption and hot gas in the Galaxy include studies of the low-redshift Lyβ forest (Shull et al. 2000a), Milky Way halo gas (Savage et al. 2000; Shull et al. 2000b), high velocity clouds (HVCs; Sembach et al. 2000b, 2001; Richter et al. 2001b), and the individual sight lines toward H 1821+643 (Oegerle et al. 2000), PG 0804+761 (Richter et al. 2001a), and PG 0953+415 (Savage et al. 2001a).

In this paper, we use *FUSE* data to investigate the IGM and ISM along the 3C 273 sight line. In §2 we describe the observations and data reduction procedures. Section 3 contains information

about absorption features in the *FUSE* spectra, including equivalent width measurements, column density derivations, and models used to describe the absorption lines. In §4 we present results for the intergalactic absorption along the sight line, and in §5 we describe the Milky Way absorption. Section 6 contains a discussion of these results. Section 7 consists of a brief summary of the scientific results of this investigation.

2. Observations

2.1. Far Ultraviolet Spectroscopic Explorer Observations

FUSE contains four Rowland circle spectrographs that produce spectra over the wavelength range 905–1187Å. Two of the spectrographs have optics (a holographically-ruled diffraction grating illuminated by an off-axis paraboloid mirror) coated with Al+LiF for greatest sensitivity above ~ 1000Å, and two have optics coated with SiC for maximum sensitivity below ~ 1000Å. The dispersed spectra from the four channels (LiF1, LiF2, SiC1, SiC2) are recorded by two delay-line microchannel-plate detectors, each individually covering nearly the full *FUSE* bandpass. Descriptions of the *FUSE* instrumentation and its on-orbit performance are given by Moos et al. (2000) and Sahnow et al. (2000a,b).

We obtained a 42.2 ksec observation of QSO 3C 237 consisting of 30 individual exposures on 2000 April 23, with the light of the quasar centered in the large ($30''\times30''$) apertures of the four optical channels. During the course of the observation, the light remained centered in the LiF1, LiF2, and SiC2 apertures but moved in and out of the SiC1 aperture due to thermally-induced image motions in the optical system. As a result, the net exposure time in the SiC1 channel was only 12.6 ksec, and the resulting SiC1 spectral resolution was degraded slightly. Most of the observation (~ 30 ksec) took place during orbital night.

We processed the data using the standard CALFUSE (v1.8.7) pipeline software available at the Johns Hopkins University in November 2000. The software screened the raw photon address lists for valid events satisfying constraints imposed for Earth limb avoidance, South Atlantic Anomaly passage, and pulse height distribution. It also corrected for large scale geometric distortions in the detector grid, changes in spectral positions on the detector due to minute grating movements induced by thermal variations, Doppler shifts caused by orbital motion of the satellite, and detector background noise (which is minimal at the flux levels considered in this study). The two-dimensional astigmatic spectra were extracted with a slit width appropriate for the spectral height at each wavelength. There was no explicit correction for the astigmatism available at the time of processing, which resulted in a slightly lower spectral resolution than could be achieved if the spectra were rectified before being summed in the spatial direction. By spreading the spectral information over many detector pixels in the spatial direction, however, the astigmatism reduces the detector fixed-pattern noise in the extracted one-dimensional spectra. No explicit flat-field corrections were applied in the standard *FUSE* processing, so we made use of the overlapping wavelength coverage

of the different channels to determine whether fixed-pattern noise artifacts affect the lines used in the analysis described in §3 and §4.

We determined the zero point of the wavelength scale by registering the molecular (H_2) and neutral and singly ionized atomic lines (Si II λ1020.699; Ar I λ1048.220, 1066.660; Fe II λ1125.448, 1143.226, 1144.938) in the spectrum to the longer wavelength S II λ1250.584, 1253.811 lines observed with the Hubble Space Telescope (*HST*) and the H I 21 cm emission profile observed with the NRAO 140' telescope (Murphy, Sembach, & Lockman, unpublished). We found that in some wavelength regions (e.g., $\sim 1040 - 1070$ Å) there is a slight offset of the interstellar lines from similar lines at other wavelengths. This may be due to a slight stretch in the wavelength dispersion solution introduced by alignment differences between the wavelength calibration spectra and the 3C 273 spectrum, detector non-uniformities, or other unknown causes. Whenever possible, we have corrected for these relative wavelength shifts and believe that the residual uncertainties are of the order of $\lesssim 8$ km s^{-1} (1σ). There is no evidence that these uncertainties are present on wavelength scales comparable to the widths of the observed absorption lines (i.e., the line profile shapes are not affected by uncertainties in the wavelengths).

The *FUSE* data are oversampled at the current instrumental resolution. Therefore, we re-binned the fully-sampled (~ 0.0065 Å pix^{-1}) data by a factor of 3, which results in $\sim$3–4 bins per $\sim$17–22 km s^{-1} resolution element. The data have $S/N \approx 15 - 35$ per resolution element, depending upon wavelength and detector segment.

The fully reduced data are shown in Figure 1, in which we plot the spectra from the detector segments having the highest signal-to-noise ratio. The coverage shown is as follows: SiC1A (1079 – 1089 Å), SiC1B ($\lambda \leq 992$ Å), SiC2A ($\lambda \leq 1001$ Å), SiC2B (1075 – 1088 Å), LiF1A (994 – 1081 Å), LiF1B (1095 – 1186 Å), LiF2A (1088 – 1182 Å), and LiF2B (999 – 1073 Å). In general, the SiC2 data are of better quality than the SiC1 data for this observation because of the alignment difficulties encountered for the SiC1 channel. Prominent interstellar and intergalactic absorption lines are indicated by tick marks above the spectra and are identified to the right of each panel. Many H_2 lines in rotational levels $J = 0 - 3$ are indicated; some of the weaker lines in these levels overlap other stronger features and are not explicitly marked. The expected locations of weak intergalactic features that are not readily apparent in the spectra are identified with an additional "?" appended to the redshift. At some wavelengths, fixed-pattern noise (FPN) features are present (e.g., 997.2 Å, 1060.7 Å 1070.9 Å, 1140.5 Å, and 1151.9 Å) as evidenced by their appearance in one channel but not the others. The broad shallow flux enhancement between 1155 and 1165 Å in the LiF1B channel is due to the optical anomaly involving the microchannel-plate grid wires as noted by Sahnow et al. (2000a).

2.2. Hubble Space Telescope Observations

The archival Goddard High Resolution Spectrograph (GHRS) observations of 3C 273 used in this work include data taken with the G160M first-order grating covering the wavelength ranges 1214–1425 Å and 1521–1572 Å, and data taken with the Ech-A echelle-mode grating covering the wavelength range 1250–1257 Å. The G160M observations include data taken as part of HST programs GTO1140, 3951, 4883 ; the Ech-A data were taken under program GO5719. (Ray Weymann was the principal investigator on all of these archival *HST* datasets.) The G160M observations were obtained before the installation of COSTAR and have been described in a number of papers (e.g., Brandt et al. 1993, 1997; Penton et al. 2000b). The post-COSTAR Ech-A observations, which include 10 separate exposures totaling 19.6 ksec, are described here for the first time.

The basic calibration and processing of these datasets followed the method described by Howk, Savage, & Fabian (1999), with the exception of refinements to the wavelength scale described below. All observations were taken with the large ($2'' \times 2''$) science aperture of the GHRS using focal plane motions to mitigate the effects of fixed-pattern noise. For data of relatively low signal-to-noise (S/N), the fixed-pattern noise in the GHRS data is a small contribution to the total error budget. While one can solve explicitly for the fixed-pattern noise spectrum and remove it from the data, we applied this correction only in cases where the fixed-pattern noise obviously affected absorption lines of interest to avoid adding extra noise into the data as part of the fixed-pattern reconstruction procedure. The processed G160M data have $S/N \sim 8 - 14$ per resolution element, with the exception of the observations of Si IV 1402 which have $S/N \sim 23$. The GHRS G160M data have a wavelength-dependent resolution of ~ 19 km s^{-1} (FWHM) at 1214 Å and ~ 14 km s^{-1} (FWHM) at 1550 Å. The Ech-A observations have a resolution of ~ 3.5 km s^{-1} (FWHM) and $S/N \sim 14$.

The absolute wavelength scale used in the standard GHRS pipeline processing is accurate to roughly ± 1 resolution element. To place all of the GHRS data on a self-consistent scale, which we also used to set the zero point of the *FUSE* wavelength scale, we used a "bootstrapping" technique. For a velocity reference, we adopted the S II $\lambda\lambda 1250.584, 1253.811$ lines observed with the Ech-A grating. These S II lines have a wavelength solution accurate to ± 3.5 km s^{-1} and contain a sharp, narrow component at $v_{LSR} = -6$ km s^{-1} that coincides with the peak of the H I 21 cm emission along the sight line. We used the Ech-A S II profiles to bring the G160M observations of the same S II lines into the LSR reference frame. The G160M observations of the S II lines also contain the Si II 1260.422 Å transition, which we used to register the Si II lines at 1304.370 Å and 1526.707 Å. The relative wavelength calibration was carried out using the ISM and IGM lines in the wavelength regions covered by the G160M observations; the only exceptions to this approach were the observations centered near the interstellar Si IV $\lambda\lambda 1393.755, 1402.770$ lines, which we tied into this self-consistent scale by assuming the 1402.770 Å line has a velocity similar to that of the interstellar C IV lines. (We did not use the stronger Si IV $\lambda 1393.755$ transition for this purpose since it is strongly blended with an IGM Lyα absorber.)

3. Measurements

We identified all of the absorption lines in each of the $FUSE$ channels using the atomic line list compiled by Morton (1991) and the H_2 line lists published by Abgrall et al. (1993a,b). We also searched for intergalactic lines of H I, O VI, and C III corresponding to known $Ly\alpha$ absorption lines having rest frame equivalent widths[5] $W_r \gtrsim 50$ mÅ (i.e., N(H I) $\gtrsim 10^{13}$ cm^{-2}).

3.1. Interstellar Lines

We estimated continuum levels for the interstellar atomic and H_2 lines by fitting spectral regions within a few hundred km s^{-1} of the lines with low-order ($n \leq 5$) Legendre polynomials. Continuum-normalized profiles for a selected set of lines are shown in Figure 2 as a function of velocity in the local standard of rest (LSR) reference frame[6]. Only the data from the channel yielding the best combination of S/N and resolution are shown. Absorption features due to other lines, including H_2, occur within ± 300 km s^{-1} of many of the lines shown. These nearby lines are identified immediately above or below each spectrum.

We measured total line equivalent widths (W_λ) and their associated errors using the procedures described by Sembach & Savage (1992). The equivalent widths of the interstellar atomic lines are tabulated in Table 1. The two equivalent width entries for each line correspond to the values derived from the data for the two most sensitive channels (LiF1 and LiF2, or SiC1 and SiC2). In general, these independent equivalent widths are in excellent agreement. The 1σ errors on the measurements were generally taken to be the larger of the formal errors derived from the integration or 10 mÅ. This latter value was adopted as a lower limit to account for the possible fixed-pattern noise contributions that could be present over the $\sim 100 - 150$ km s^{-1} integration range of the equivalent width measurements (see Table 1).

For the O VI $\lambda1031.926$ line, we split the equivalent width integration into two velocity ranges (-160 to $+100$ km s^{-1} and $+100$ to $+240$ km s^{-1}) because the O VI profile contains a broad, positive velocity wing that is not seen in any other atomic species. The high velocity absorption cannot be easily modeled as a lowering of the QSO continuum at these wavelengths; on the contrary, its existence appears quite robust to reasonable continuum placements derived from adjoining spectral regions. The total interstellar O VI $\lambda1031.926$ equivalent width is 450 ± 15 mÅ.

Most of the molecular hydrogen lines identified in Figures 1 and 2 are readily distinguished from

---

[5]Throughout this work, we use the notation W_{obs} to indicate the $observed$ equivalent width of a line and W_r to indicate the $rest\ frame$ equivalent width of a line. The relationship between the two quantities is given by $W_{obs} = (1 + z)W_r$, where z is the redshift of the absorption. For the Milky Way ISM lines, $W_\lambda = W_{obs}$.

[6]The heliocentric to LSR correction in the direction of 3C 273 is $v_{LSR} = v_{helio} + 2.8$ km s^{-1}, assuming a solar motion of 16.5 km s^{-1} in the direction $l = 53°$, $b = +25°$(Mihalas & Binney 1981).

the atomic interstellar and intergalactic lines. However, there are numerous cases where weaker H_2 lines from rotational levels $J = 3 - 4$ may contribute to the observed absorption (see §4 and §5.1). We have therefore listed in Table 2 the observed equivalent widths (or limits) for several transitions in the $J = 3 - 4$ rotational levels. The lines listed have f-values that span those of the $J = 3 - 4$ lines discussed later in conjunction with blending issues associated with the IGM measurements. No $J = 4$ lines are positively detected in the $FUSE$ data down to a 3σ limit of $\approx 30\,\mathrm{m\AA}$ [$N(H_2)$ $\sim (2 - 3) \times 10^{14}\,\mathrm{cm}^{-2}$]. We list the 3σ column density limits derived for the H_2 lines in the last column of Table 2, assuming a linear curve-of-growth relation between W_λ and N.

3.2. Intergalactic Lines

Numerous intergalactic absorption lines are present in the $FUSE$ spectra of 3C273. We measured the equivalent widths of these lines in the same manner as for the interstellar lines (§3.1). In Table 3 we list the rest wavelengths, observed wavelengths, and observed equivalent widths on both detectors for each IGM line for which the corresponding Lyα equivalent width is greater than 50 mÅ. The entries include values for H I Lyβ (and Lyγ when appropriate), O VI $\lambda\lambda 1031.926, 1037.617$, and C III $\lambda 977.020$ for the absorbers at $z = 0.00338, 0.00530, 0.02497,$ 0.04898, 0.06655, 0.09012, 0.12007, and 0.14660. For completeness, we also list the equivalent widths of the Lyα lines measured with pre-COSTAR GHRS data in Table 3. These Lyα line strengths and redshifts are in good agreement with those made by previous investigators (e.g., Penton et al. 2000b). Comments appended to each entry provide additional information about possible blending with Galactic lines. We have listed equivalent widths for as many H I lines as are observable down to a limiting equivalent width $W_{obs} \sim 20 - 30$ mÅ (3σ).

We plot the continuum normalized IGM absorption lines in Figure 3 as a function of systemic velocity centered on the redshifts listed in Table 3. In all but two cases, the $z = 0.12007$ absorber and possibly the $z = 0.00338$ absorber, there is no significant metal-line absorption detected. Confusion with Galactic lines is problematic for some of the IGM lines. We discuss possible blends with Galactic features for each system in the following section.

4. Intergalactic Medium Absorption

A summary of the IGM column densities for all of the absorbers studied is provided in Table 4. Column densities for H I were derived by fitting a single-component Doppler-broadened curve of growth to the H I lines detected in each absorber. Data points from independent channels were included in the error-weighted fits whenever possible. We followed the procedures outlined by Savage, Edgar, & Diplas (1990) for calculating errors on $N(H\,I)$ and $b(H\,I)$. Limits on $N(O\,VI)$ and $N(C\,III)$ are conservative 3σ estimates derived from the data in the channel having the highest sensitivity. If data from both the LiF1 and LiF2 channels are considered, these limits translate into

$\sim 4\sigma$ estimates. We now discuss each of the absorbers individually.

4.1. Virgo Cluster Absorbers ($z = 0.00338$ and $z = 0.00530$)

The 3C 273 sight line passes through the Virgo Cluster. The two strongest Lyα absorbers along the sight line occur at velocities representative of those of the cluster ($\langle V \rangle \approx 1141 \pm 60$ km s^{-1}; $\sigma_r \approx 666$ km s^{-1}; Tammann 1972). We detect redshifted Lyβ absorption associated with both clouds at $z = 0.00338$ ($cz \approx 1015$ km s^{-1}) and $z = 0.00530$ ($cz \approx 1590$ km s^{-1}). Previous observations of the Lyβ lines with $ORFEUS\text{-}II$ (Hurwitz et al. 1998) confirmed the intergalactic identification of the longer wavelength Lyα lines observed with the HST by Morris and co-workers but were of insufficient quality to determine the H I column densities of the absorbers to a high degree of confidence.

The Lyα lines for the two Virgo absorbers have similar equivalent widths (~ 370 m Å), but the Lyβ lines differ in equivalent width by $\sim 90 - 100$ m Å and have very different shapes (Figure 3). Note that the measured depth of the Lyβ line of the 1590 km s^{-1} absorber is greater than the depth of the Lyα line; this is due to the large instrumental smearing of the Lyα line resulting from the spherical aberration of the pre-corrected HST optics. There is little or no detectable Lyγ absorption in the lower velocity cloud (Table 3), but the 1590 km s^{-1} cloud can be seen in absorption through the Lyman series up to Lyθ without much confusion by Galactic absorption. These higher-order H I lines are identified in Figure 1 and are plotted as a function of systemic velocity in Figure 4.

The Lyβ lines of both Virgo absorbers occur at wavelengths where weak Galactic H$_2$ absorption may blend with the lines. We show the Lyman series H$_2$ (6–0) R(3) and P(3) lines in Figure 5 together with an assortment of R(3) and P(3) lines in other vibrational bands having line strengths, $f\lambda$, spanning those of the (6–0) lines. The top spectra in the two panels of Figure 5 contain the Virgo Lyβ lines with fits to the R(3) and P(3) lines shown as heavy smooth curves. Nearby R(2) and P(2) lines confirm the velocities of the $J = 3$ lines relative to the IGM lines. For the 1015 km s^{-1} absorber, the overlapping H$_2$ R(3) line has an (unblended) equivalent width of ≈ 42 mÅ and contributes ≈ 25 mÅ to the observed (blended) absorption. For the 1590 km s^{-1} absorber, the overlapping H$_2$ P(3) line has an equivalent width of ≈ 34 mÅ and contributes ≈ 16 mÅ to the observed absorption.

We show the H I curves of growth for the two Virgo absorbers in Figure 6. The COG results for the 1015 km s^{-1} absorber differ only slightly from those derived by Weymann et al. (1995) from profile fitting of the Lyα line alone[7]: $\log N(\text{H I})_{COG} = 14.40 \pm 0.10$ versus $\log N(\text{H I})_{Ly\alpha} = 14.19 \pm 0.04$, and $b_{COG} = 30.3^{+4.3}_{-3.8}$ km s^{-1} versus $b_{Ly\alpha} = 40.7 \pm 3.0$ km s^{-1}. However, the COG results for the 1590 km s^{-1} absorber differ greatly from those derived previously from Lyα profile

---

[7]Unless otherwise indicated, errors quoted in this paper are 1σ (68% confidence) estimates.

fitting: $\log N(\text{H I})_{COG} = 15.85^{+0.10}_{-0.08}$ versus $\log N(\text{H I})_{Ly\alpha} = 14.22 \pm 0.07$, and $b_{COG} = 16.1 \pm 1.1$ km s^{-1} versus $b_{Ly\alpha} = 34.2 \pm 3.3$ km s^{-1}. Curve-of-growth column densities and b-values for the 1590 km s^{-1} absorber were derived both including and excluding the Lyα line. The slight excess of Lyα equivalent width in the 1590 km s^{-1} absorber over that predicted by the best-fit curve of growth to the H I lines in the *FUSE* bandpass (Figure 6) is most likely caused by an additional low column density absorption observable in Lyα that is essentially undetectable in the higher order H I lines. The excess is $\lesssim 40\,\text{m\AA}$. Including Lyα in the curve-of-growth analysis increases the derived b-value by ≈ 1.5 km s^{-1} and decreases the derived column density by ≈ 0.08 dex (see Table 4), which is consistent with the column derived solely from the higher order H I lines observed by *FUSE* to within the uncertainties of each estimation. Higher resolution Lyα observations are needed to determine whether this absorber has a multi-component structure as implied by the single-component COG analysis. The extant GHRS data are insufficient to determine the detailed velocity structure of the Lyα absorption since the instrumental line spread function is a complex convolution of both a narrow core and broad wings.

In summary, we find the following relationships between our COG values and previous determinations of N and b in the Virgo absorbers:

$$cz \sim 1015 \text{ km s}^{-1} : \qquad \left(\frac{\log N_{COG}}{\log N_{Ly\alpha}}\right) \approx 1.6, \qquad \left(\frac{b_{COG}}{b_{Ly\alpha}}\right) \approx 0.7 \tag{1}$$

$$cz \sim 1590 \text{ km s}^{-1} : \qquad \left(\frac{\log N_{COG}}{\log N_{Ly\alpha}}\right) \approx 43, \qquad \left(\frac{b_{COG}}{b_{Ly\alpha}}\right) \approx 0.5 \tag{2}$$

Synthetic line profiles constructed using the best fit curve-of-growth results are overplotted on the 1590 km s^{-1} absorber H I lines in Figure 4. The synthetic profiles have been convolved with a single-component Gaussian instrumental line spread function having a fixed width of FWHM $= 0.075\,\text{\AA}$. The general agreement with the observed profiles is excellent; the minor differences observed could be reduced through the application of a wavelength-dependent line spread function.

Unfortunately, it is not possible to unambiguously associate the observed absorbers with any particular galaxy within the Virgo Cluster since the internal cluster velocity dispersion is sufficiently high that numerous galaxies could be responsible for the absorption. McLin et al. (2001) have found a galaxy with a redshift of 1512 ± 40 km s^{-1} that seems to be a plausible source for the 1590 km s^{-1} absorber.

The two Virgo absorbers contain metals. We detect very weak O VI $\lambda 1031.926$ absorption in the 1015 km s^{-1} absorber (Figure 3 and Table 3). The absorption is present in both LiF channels but is weak. The conservative errors of 10 mÅ in both channels account for statistical noise, continuum placement, and fixed-pattern noise uncertainties. The Lyman series H_2 (6–0) R(3) absorption due to the Milky Way ISM is expected to be weak and offset from this absorption. Based on the FUSE data, we estimate $N(\text{O VI}) \approx (2.1\pm0.8) \times 10^{13}$ cm^{-2}. This is the lowest redshift IGM O VI absorber outside the Local Group.

There is no obvious O VI associated with the 1590 $km\,s^{-1}$ absorber in the 1037.617 Å line. We place a 3σ limit of N(O VI) $< 4.8 \times 10^{13}$ cm^{-2} on the presence of O VI. The O VI λ1031.926 and C III λ977.020 lines are blended with Milky Way ISM absorption (Table 3). Using the H_2 parameters discussed in §5.2.3 to deblend the line, we conservatively estimate that N(C III) $\lesssim 1.2 \times 10^{13}$ cm^{-2} (3σ), which translates into N(H$^+$) $\lesssim 3.2 \times 10^{16}Z^{-1}$ cm^{-2} under the assumption that all of the carbon is in the form of C III. Here, Z is the metallicity in units of the solar metallicity. Thus, N(H$^+$)/N(H I) $\lesssim 4.5Z^{-1}$. Williger et al. (2001) detect Si III λ1206.500 absorption, which confirms that ionized gas is present. Additional searches for other strong ionized gas lines in the *HST* bandpass (e.g., Si IV, C IV) would help to constrain the ionized gas content of both Virgo absorbers.

4.2. The $z = 0.02947$ absorber

This absorber exhibits very weak Lyβ absorption present at the 2-3σ level associated with the 139 mÅ Lyα absorber. The ratio of Lyα to Lyβ can be used to determine a reliable H I column density, since an optically thin absorber would have a Lyβ equivalent width of W_λ(Lyα) / 7.4 $\approx$ 19 mÅ, which is consistent with the observed value of 22 ± 9 mÅ averaged over the two LiF channels. We find N(H I) ≈ 13.55 (Table 4). Since the b-value is not constrained by the Lyα/Lyβ equivalent width ratio, we fit a single Voigt profile to the GHRS Ech-A Lyα profile shown in Figure 3 to estimate $b = 38.7 \pm 1.7$ $km\,s^{-1}$. This b-value is similar to the value of 36 $km\,s^{-1}$ suggested by Morris et al. (1991) using the pre-COSTAR GHRS G160M data but is substantially smaller than the value of 61 ± 8 $km\,s^{-1}$ found by Penton et al. (2000b) with the same G160M dataset.

To the best of our knowledge, the Ech-A profile shown in Figure 3 is the highest resolution absorption profile available for any IGM Lyα line at low-moderate redshift ($z \lesssim 1.5$). Unless the gas is cold ($T \lesssim 300$ K), which seems unlikely, the GHRS Ech-A data fully resolve the H I absorption. No more than $\sim 10\%$ of the total column density can be in any single component with $T < 1000$ K. There is noticeable structure within the profile; binning the data by a factor of 2 (to an effective resolution of about 7 $km\,s^{-1}$ FWHM) suggests that there may be both a narrow ($b \sim 25$ $km\,s^{-1}$) core containing about 30% of the column and a broader ($b \sim 50$ $km\,s^{-1}$) component containing about 70% of the column. This has important implications, since the broad component could have a temperature as high as $\sim 1.5 \times 10^5$ K if the broadening is thermal in nature. (Even if only a single component is fit, the temperature could be as high as $\sim 10^5$ K.) Alternatively, if the broadening is non-thermal, there must be significant bulk or turbulent motions within the absorber. Higher S/N observations of the Lyα line at comparable resolution with STIS could be used to check the validity of this claim and to search for metal-line diagnostics of 10^5 K gas (e.g., C IV) if the gas is predominantly collisionally ionized. No C III or O VI absorption is detected in the *FUSE* spectra of this absorber.

4.3. The $z = 0.04898$ absorber

This absorber has an observed Lyα equivalent width of ≈ 126 mÅ, and like the $z = 0.02947$ system, the absorption is confirmed to be optically thin by the absence of a strong Lyβ absorption. There is a hint of Lyβ absorption in the LiF1 data (Figures 1 and 3), but the observed wavelength of 1075.95 Å is not covered by the LiF2 channel. The O VI lines fall in the *FUSE* LiF wavelength coverage gap, so the only measurements available come from the lower S/N SiC data (Table 3). The C III line in this absorber falls in the wing of Galactic Lyβ absorption and is not observable.

4.4. The $z = 0.06655$ absorber

This is the fourth strongest Lyα absorber along the sight line, with an observed equivalent width of ≈ 312 mÅ. The corresponding Lyβ absorption is recorded only in the LiF2 channel because it falls in the SiC1/LiF1 wavelength gap. The line is partially blended with the Galactic H$_2$ (1–0) P(1) line (Figure 3). Lyγ occurs near 1037.3 Å and is blended with Galactic C II and H$_2$ absorption. There is no detectable C III or O VI in this absorber.

4.5. The $z = 0.09012$ absorber

This absorber has a very shallow, irregularly shaped Lyα line extending over nearly 200 km s^{-1}. There may be very weak Lyβ absorption at the 2-3σ level consistent with an optically thin cloud. There is no detectable O VI absorption. C III is blended with the Galactic H$_2$ (3–0) R(2) line, which we modeled; we find no residual C III down to a level of < 30 mÅ (3σ).

4.6. The $z = 0.12007$ absorber

This absorber has a modest H I column density, $\log N(\text{H I}) = 13.61$, and significant detections of O VI and C III. The metal-line absorption is weak [W_{obs}(O VI λ1031.926) ≈ 30 mÅ], but is present in both *FUSE* channels (Table 3) as well as in the weaker λ1037.617 line. The C III line falls near a blend of Galactic H$_2$ and IGM Lyβ absorption at a redshift $z = 0.06655$ (see Figure 3).

We find N(O VI) $\approx (2 - 3) \times 10^{13}$ cm^{-2}, which is smaller than the columns for other O VI absorbers detected with *FUSE* in the spectrum of PG 0953+415 (see Savage et al. 2001a). We find N(H I)/N(O VI) $= 1.7 \pm^{0.6}_{0.8}$, indicating that the gas is essentially fully ionized if the H I and O VI are co-spatial. For an O VI ionization $O^{+5}/O \leq 0.2$, the observed value of N(O VI) $= 2.4 \times 10^{13}$ cm^{-2} implies N(H$^+$) $\geq 1.6 \times 10^{17} Z^{-1}$ cm^{-2}, where Z is the metallicity of the gas[8]. Thus, N(H$^+$)/N(H I) $\gtrsim 4000 Z^{-1}$. Additional ultraviolet data for other ionized species (e.g., C IV,

N V) would be valuable in determining the ionization and metallicity of the gas.

The nearest known galaxy to the sight line with a redshift within a few hundred $km\,s^{-1}$ of the absorber lies at a projected distance of ~ 2.5 Mpc from the 3C 273 sight line assuming $H_0 = 65$ $km\,s^{-1}\,Mpc^{-1}$ and has a redshift $z = 0.12067$ (Morris et al. 1993). McLin et al. (2001) have also found a galaxy at $z = 0.12026$ that is $\sim 16'$, or ~ 2.6 Mpc, from the sight line.

4.7. The $z = 0.14660$ absorber

The Lyα line for this absorber occurs at a wavelength of 1393.89 Å and is blended with Galactic Si IV $\lambda 1393.755$ absorption. Our estimate of the observed equivalent width of the line ($355 \pm 20\,$mÅ) is in good agreement with the value of $331\,$mÅ derived by Morris et al. (1991) but differs substantially from the value of $216\,$mÅ quoted by Savage et al. (1993)[9]. We re-derived the Lyα profile by scaling the observed optical depth of the "clean" Galactic Si IV $\lambda 1402.770$ line by a factor of 2, subtracting this scaled optical depth from the observed optical depth of the Si IV + Lyα blend, and recalculating the absorption profile of the residual (e.g., IGM Lyα) absorption. We show our decomposition of the absorption profile in Figure 7.

We detect Lyβ absorption in this absorber with an equivalent width consistent with an optically thin cloud. This is the third strongest H I absorber along the 3C 273 sight line. There are no detectable O VI or C III absorptions associated with the intergalactic H I at this redshift.

5. Milky Way Interstellar Absorption

The 3C 273 sight line passes through the ISM of the Galactic disk and halo. In this high latitude direction ($l = 289.95°, b = +64.36°$), Galactic rotation does not strongly affect the radial velocity of the interstellar gas; for $d < 10$ kpc, the expected LSR velocities of a smoothly distributed medium corotating with the Galactic disk lie between 0 and -8 $km\,s^{-1}$. The most notable features along or near the sight line include radio continuum Loops I and IV (Berkhuijsen 1971) and the North Polar Spur, which is seen in both 21 cm emission (Colomb, Poppel, & Heiles 1980; Heiles et al. 1980) and in X-ray emission (McCammon et al. 1983; Snowden et al. 1995). Descriptions

---

[8]The peak O VI ionization fraction of ~ 0.2 occurs in collisional ionization equilibrium at a temperature of $\sim 3 \times 10^5$ K (Sutherland & Dopita 1993). This ionization fraction is also rarely exceeded if the gas is photoionized under conditions that might be found in the low-redshift IGM.

[9]The lower equivalent width quoted by Savage et al. (1993) resulted from a minor mathematical error in the scaling of the deblended IGM and Milky Way absorption features. Figure 7 in that paper can be compared to our revised deblending shown in Figure 7 of this paper. In both the present paper and in the Savage et al. (1993) article, this error does not affect the conclusions regarding the column density or velocity of Si IV, since that information is based in both studies on the 1402.770 Å line.

of these features and an overview of the ultraviolet and optical absorption along the sight line are given by Savage et al. (1993). Here, we summarize some of the new information about the interstellar gas obtained from the *FUSE* spectra of 3C 273.

5.1. Kinematics

The neutral and low ionization interstellar gas toward 3C 273 occurs in two main groupings of clouds centered at $v_{LSR} \approx -15$ and $+23$ km s^{-1}, as derived from high resolution GHRS observations of the S II $\lambda\lambda 1250.584, 1253.811$ lines and *FUSE* observations of P II $\lambda 1152.818$, Si II $\lambda 1020.699$, and Fe II $\lambda 1121.975, 1125.448, 1143.226, 1144.938$. These absorption features are shown in Figure 8 along with the H I 21 cm emission profile obtained with the NRAO 140-foot telescope. The ultraviolet absorption in the neutral and singly ionized species occurs at velocities for which H I 21 cm emission is also detected. The -15 km s^{-1} grouping is the dominant contributor to both the 21 cm emission and the ultraviolet absorption. The maximum H I emission occurs at $v_{LSR} \approx -6$ km s^{-1}, the velocity of the strong, sharp absorption feature visible in the S II $\lambda 1250.584$ line shown near the bottom of Figure 8.

The S II profiles observed at high resolution with the GHRS indicate that the velocity component distributions of the low ionization groups of clouds are complex. The negative velocity grouping contains at least three components, and the positive velocity grouping contains at least two components. Typical b-values of Gaussian components fit to the profiles are $\sim 3 - 8$ km s^{-1}. The profiles are sufficiently complicated that it is difficult to obtain a unique solution to the various component parameters; this is particularly true for the negative velocity (-15 km s^{-1}) group, which has a trailing absorption shoulder that is difficult to describe as a sum of discrete Gaussian components (see Figure 8). Comparisons of the apparent column density profiles (next section) for the S II lines shows, however, that there is unlikely to be any unresolved saturated structure within the lines, except possibly in the narrow core at -6 km s^{-1}.

The overall shape of the absorption lines is consistent from species to species, with the possible exception of the Ar I $\lambda\lambda 1048.220, 1066.660$ lines. The Ar I profiles consist of a two-component structure, but the cloud group centroids are separated by only ~ 33 km s^{-1}, compared to ~ 38 km s^{-1} for the "dominant" ion lines of Si II, P II, S II, and Fe II. This appears to be due primarily to a shift of the redward Ar I cloud grouping to slightly less positive velocities compared to the other species. Such an offset could be due to differences in the ionization of the components within the positive velocity clouds. For example, if the higher velocity components in the group contain a significant amount of ionized gas, then Ar I, which is found predominantly in the neutral gas and is particularly susceptible to photoionization compared to other neutral species (Sofia & Jenkins 1998), may have a different profile shape than the singly ionized species.

The H_2 absorption along the sight line occurs near the velocities of the positive velocity cloud group seen in the neutral and singly ionized atomic lines. The H_2 is centered on an LSR velocity

of $+16$ km s^{-1}, slightly less than the velocity of the low ionization lines (see Figure 8). There is little detectable H$_2$ absorption near -15 km s^{-1}. Thus, the primary molecular absorption along the sight line does not coincide with the peak atomic column density concentration (in velocity) along the sight line. This runs somewhat contrary to expectations and indicates that it is not always possible to use the peak of the H I 21 cm emission to set the zero-point of the velocity scale for the H$_2$ absorption observed with *FUSE*.

The profiles of the doubly ionized species observed along the sight line (S III, Fe III) span velocities similar to those covered by the singly ionized lines (see Figure 2). The S III and Fe III lines are smoother than their singly ionized counterparts, indicating that these ions may trace both the structured absorption as well as a more turbulent medium. Because of its great strength, the C III $\lambda977.020$ line is broader than the S III or Fe III lines. It has an extent (FWHM ≈ 180 km s^{-1}) comparable to or slightly larger than that of the strong C II $\lambda1036.337$ line. The great extent of these lines implies the existence of a low column density medium that is highly turbulent.

The O VI $\lambda\lambda1031.926, 1037.617$ lines are broad and span a velocity range from -100 to $+100$ km s^{-1}. The 1031.926 Å line also reveals a broad, shallow wing of absorption between $+100$ and $+240$ km s^{-1} that is not detected in other high or low ionization species, including C II, C III, C IV, Si IV, and N V (Sembach et al. 1997). The feature cannot be redshifted H I Lyβ at $z \approx 0.00638 - 0.00685$ because there is no corresponding Lyα absorption at this redshift. Broad shallow interstellar O VI absorption features are seen in several other directions through the Milky Way halo (e.g., toward Mrk 1383, PKS 2005-489; Savage et al. 2001b). Toward 3C 273, the wing contains roughly 13% of the total O VI equivalent width. The positive velocity wing of the O VI $\lambda1037.617$ line is blended with absorption by the nearby Lyman H$_2$ (5–0) R(1) line. The O VI lines do not contain any unresolved saturated component structure.

5.2. Column Densities and Elemental Abundances

We computed column densities for the interstellar species observed toward 3C 273 by fitting single-component Doppler-broadened curves of growth to the equivalent widths listed in Table 1 and by calculating the apparent optical depths (AOD) of the lines (Savage & Sembach 1991). We list the column density results in Table 5 for several species. Values are listed for the two groups of components near -15 and $+23$ km s^{-1} as well as for the entire sight line. The velocity ranges considered were similar to those listed in Table 1 for the individual lines.

The apparent column density obtained by integrating the column density profiles over velocity is given by

$$N_a = \int N_a(v)dv = \frac{3.768 \times 10^{14}}{f\lambda} \int \tau_a(v)dv \quad (cm^{-2}) \tag{3}$$

where $\tau_a(v)$ is the apparent optical depth of the line (equal to the natural logarithm of the estimated continuum divided by the observed intensity) at velocity v (in km s^{-1}), f is the oscillator strength

of the line, and λ is the wavelength of the line (in Å).

5.2.1.   Neutral and Low Ionization Gas

The total amount of neutral (H I) gas along the 3C 273 sight line can be estimated in several ways. Two independent estimates are provided in Table 5. The first of these is an estimate based upon an integration of the 21 cm emission profile shown in Figure 8 over the velocity ranges from -50 km s^{-1} to $+10$ km s^{-1} and from $+10$ km s^{-1} to $+60$ km s^{-1} under the assumption that the emission is optically thin (see eq. 3-38 in Spitzer 1978). The total resulting column density is $\log N(\text{H I}) = 20.23$. The second estimate is based upon a profile fit to the radiation damping wings of the Lyβ line shown in Figure 1. The resulting column density is $\log N(\text{H I}) = 20.20 \pm 0.05$. Both results are consistent with each other and with the strengths of the higher order Lyman series lines observed in the *FUSE* bandpass. The higher order lines lie on the flat part of the curve of growth and are often contaminated by metal lines, molecular hydrogen lines, and geocoronal airglow emission.

Comparisons of the apparent column density profiles for each species revealed that many of the low ionization lines contain unresolved saturated structures at the resolution of the *FUSE* data. The weak-line apparent column density integrals for the Fe II lines indicated that lines having apparent optical depths $\tau_a \lesssim 1$ yield the same integrated column density as derived from the COG. Thus, the AOD results for species having weak lines of comparable optical depth (like P II λ1152) should be reliable provided that the velocity structure is similar to that of Fe II. To help constrain the b-values derived from the COG for Si II and Fe II, we used the equivalent width measurements reported by Savage et al. (1993) for several strong lines of these species observed with the *HST/GHRS* (see Table 5 notes). The S II results derived here from high-resolution GHRS Ech-A data are much more accurate than previous values derived from the G160M data; we find a sight line total column density of $\log N(\text{S II}) = 15.46 \pm 0.06$, compared to the value of $15.60^{+0.24}_{-0.15}$ derived by Savage et al. (1993).

A standard uncertainty in deriving accurate estimates of the relative elemental abundances is determining to what extent ionization affects the column densities of the different ionization stages of each element observed. The relative gas-phase abundance of elements "X" and "Y" is usually written as

$$[X/Y] = \log N(X^i) - \log N(Y^j) - (A(X) - A(Y)), \qquad (4)$$

where X^i and Y^i are usually the neutral or singly ionized forms of X and Y, and $A(X)$ and $A(Y)$ are the cosmic (solar) abundances of X and Y on a logarithmic scale where $A(\text{H}) = 12.00$. In most abundance studies, the total H II column density is unknown, so it is often assumed that singly ionized species trace mostly neutral (H I) gas and little ionized (H II) gas.

Using *FUSE* observations of both singly and doubly ionized atoms of the same element, we can check the validity of the above assumption and its impact on the elemental abundance estimates.

The doubly ionized forms of Fe and S are not present in appreciable quantities in H I regions $(IP_{Fe\,II} = 16.18$ eV and $IP_{S\,II} = 23.33$ eV$)$[10]. We find N(Fe III)/(N(Fe II)+N(Fe III)) ≈ 0.18 and N(S III)/(N(S II)+N(S III)) ≈ 0.13. Thus, the numbers of doubly ionized atoms of Fe and S are small compared to their singly ionized counterparts.

For a warm photoionized medium characteristic of the "Reynolds Layer" having $n_e \sim 0.1$ cm^{-2} and $T \sim 10^4$ K (Reynolds 1993), the predicted ionization fractions of Fe II and Fe III are ~ 0.5 (Sembach et al. 2000a). Thus, the relative column densities of Fe II and Fe III imply that approximately 36% of the Fe along the sight line is in the warm ionized medium (WIM) if there are no other sources of ionization along the sight line. This percentage is a factor of about 1.5 higher than that derived for the sight line to vZ 1128 $(l = 42.5°, b = 78.7°$; Howk, Sembach, & Savage 2001a). However, the predicted ionization fractions of S II and S III are 0.80 and 0.20, respectively, implying that most of the S ($\sim 65\%$) is in the WIM if no other ionization sources are present. This leaves only $\sim 35\%$ of the S available for the neutral gas along the sight line, a result clearly at odds with the observed amounts of H I and P II and the implied depletion of S out of the gas-phase that would be required in the H I gas. This result strongly suggests that there must be other sources of ionization, such as shocks, that increase the amount of S III along the sight line above that expected from a pure WIM layer.

We now investigate the average degree of elemental incorporation into dust grains along the sight line for several elements, considering whenever possible the ionization stages that are dominant in both H I and H II regions. First, we compare Fe, a refractory element that is readily incorporated into dust grains, to S, an element found primarily in the gas-phase (Savage & Sembach 1996). We find N(Fe II+Fe III) / N(S II+S III) = 0.21 (Fe/S)$_\odot$, which indicates that Fe is depleted from the gas by an amount comparable to that inferred for warm clouds in the Galactic halo (Sembach & Savage 1996). Next, we consider (P/S), (Si/S), and (Ar/S); the absence of a measurement for Si III implies N(Si II+Si III) $\geq$ N(Si II). We find N(Si II+Si III) / N(S II+S III) $\geq$ 0.20 (Si/S)$_\odot$, N(P II+P III) / N(S II+S III) = (0.6–1.7) (P/S)$_\odot$, and N(Ar I) / N(S II) $\geq$ 0.45 (Ar/S)$_\odot$. The nearly solar (P/S) and (Ar/S) ratios strongly suggest that these three elements are found predominantly in the gas phase along the 3C 273 sight line. Neither P nor S is usually depleted by more than a factor of ~ 2 even in cold clouds (Jenkins 1987), and Ar is a noble element. The lower limit on (Si/S) is about a factor of two lower than typically found in Milky Way halo clouds, but would probably increase by roughly this amount if Si III could be measured.

All of the above abundance ratios are consistent with the abundances found in warm, diffuse halo clouds (Sembach & Savage 1996; Savage & Sembach 1996). The ratios for the two cloud groupings along the sight line are similar, suggesting that in both cases the absorption occurs primarily in regions where there the grain mantles have been reduced and the grain cores exposed. Furthermore, there are few differences between the ratios derived under the assumption that all of the singly ionized atoms occur in H I regions and the ratios derived from a combination of singly

---

[10]Ionization potentials in this paper are from Moore (1970).

and doubly ionized species. This implies that dust in the warm, ionized gas along this sight line has properties similar to the dust in the warm neutral gas. Finally, we note that N(S II)/N(H I) = 0.98 ± 0.16 (S/H)$_\odot$, where N(H I) is derived from the damping wings of the H I Lyβ profile shown in Figure 1 (see also Table 5). Even after accounting for some S II in ionized regions along the sight line, it is unlikely that S is depleted from the gas by more than a factor of ~ 2. We summarize the ion ratios and elemental abundance results in Table 6.

5.2.2. High Ionization Gas

A comparison of the O VI apparent column density profiles, $N_a(v)$, derived from the LiF1 data for the 1031.926 Å and 1037.617 Å lines is shown in the top left panel of Figure 9. We also plot the 1031.926 Å profile for the LiF2 channel. The good agreement of the $N_a(v)$ profiles indicates that there are no unresolved saturated structures within the lines, which implies that the observed profiles are valid, instrumentally-smoothed representations of the true column density per unit velocity. Furthermore, the broad positive velocity wing is present in all of the profiles. The width of the main O VI absorption (FWHM $\sim$ 100 km s^{-1}) is governed by thermal broadening, turbulent motions, and component structure. For gas at $T = 3 \times 10^5$ K, the temperature at which O VI peaks in abundance in collisional ionization equilibrium (Sutherland & Dopita 1993), a single component has $FWHM \approx 30$ km s^{-1}. An upper limit to the gas temperature, $T_{max} < 3.5 \times 10^6$ K is implied by the width of the O VI line core. However, it is unlikely that the gas is this hot since the fractional abundance of O VI at such high temperatures is very low $(O^{+5}/O < 2 \times 10^{-4})$.

The maximum observed optical depth of the O VI $\lambda 1031.926$ absorption is $\tau_a^{max} \approx 1.9$, so the true optical depth at line center is likely to be modest given the great breadth of the line compared to the instrumental resolution. We can rule out the presence of strong narrow components ($\tau_0 > 3$; $T < 5 \times 10^4$ K; FWHM < 12 km s^{-1}) in the $N_a(v)$ profiles based on the good agreement between the $N_a(v)$ profiles for the weak and strong lines (see Figure 9). This implies that the O VI is indeed tracing primarily hot $(T \sim 10^5 - 10^6$ K) gas.

We derive an O VI column density of $\log N$(O VI) = 14.73 ± 0.04 (-160 to $+100$ km s^{-1}) using the apparent column density profiles of the 1031.926 Å and 1037.617 Å lines. If we include the positive velocity wing in the *FUSE* measurement, we find $\log N$(O VI) = 14.77 ± 0.04 (-160 to $+240$ km s^{-1}). The O VI column density derived from *FUSE* can be compared to $\log N$(O VI) = $14.85^{+0.10}_{-0.15}$ derived from *ORFEUS-II* observations having ~ 100 km s^{-1} resolution and $\log N$(O VI) > 14.3 derived from *HUT* spectra having ~ 1000 km s^{-1} resolution (Davidsen 1993). Neither of these previous observations could resolve the weaker O VI $\lambda 1037.617$ line from neighboring absorption lines. To date, this is the highest column density of O VI measured along any sight line through the Milky Way halo.

We show the O VI apparent column density profile together with scaled profiles for N V, C IV, and Si IV from Sembach et al. (1997) in the other three panels of Figure 9. The integrated high

ion column density ratios between -100 and $+100$ km s^{-1} are:

$$\frac{N(\text{O VI})}{N(\text{N V})} = 7.2 \pm 1.1; \quad \frac{N(\text{O VI})}{N(\text{C IV})} = 1.7 \pm 0.2; \quad \frac{N(\text{O VI})}{N(\text{Si IV})} = 8.9 \pm 1.1 \tag{5}$$

The O VI, N V, and C IV high ion $N_a(v)$ profiles trace each other remarkably well, indicating that the three species arise in similar regions along the sight line. The velocity extents of the primary absorption are similar, and the profiles have similar shapes. The notable exception to this is the Si IV excess at $-7 \le v_{LSR} \le +25$ km s^{-1} compared to the other profiles. Si III has a lower ionization potential than the other highly ionized species (IP$_{\text{Si III}} = 33.5$ eV), so the abundance of Si IV is therefore much more sensitive to photoionization by starlight than the abundances of C IV, N V, and O VI. The velocities of the Si IV excess correspond to those of the positive velocity grouping of low ionization species and the H_2 along the sight line.

At the higher positive velocities of the broad O VI absorption ($+100$ to $+240$ km s^{-1}), we place the following limits (3σ) on the high ion column densities: $\log N(\text{N V}) < 13.3$, $\log N(\text{C IV}) < 13.0$, and $\log N(\text{Si IV}) < 12.9$. Combined with $\log N(\text{O VI}) = 13.71 \pm 0.05$, these values yield:

$$\frac{N(\text{O VI})}{N(\text{N V})} \ge 2.6; \quad \frac{N(\text{O VI})}{N(\text{C IV})} \ge 5.1; \quad \frac{N(\text{O VI})}{N(\text{Si IV})} \ge 6.5 \tag{6}$$

It is not possible to place a limit on C III $\lambda977.020$ at these velocities because of confusion with a strong IGM Lyγ line at $z = 0.00530$.

5.2.3. Molecular Gas

Molecular hydrogen lines are found throughout the *FUSE* spectrum of 3C 273. Although they are not the primary focus of this investigation, it is nonetheless necessary to accurately characterize the column densities in several of the rotational levels so that the impact of these lines on the absorption observed for other species can be assessed. In our census of the IGM absorbers along the sight line, the $J = 3$ rotational level lines are the most frequent Galactic absorption features that pose blending problems.

We modeled the H_2 lines in the $J = 0 - 3$ rotational levels by measuring the equivalent widths of lines free of contamination by other absorption features (see Figure 1). The lines of each level were placed on a single-component COG to estimate a column density and b-value for the molecular gas. Using this information, we constructed a synthetic H_2 spectrum and compared it to the data. We then varied the b-value and column densities of the individual levels to determine the robustness of the fit to the data and to estimate errors on the column densities. Examples of the fits obtained for several $J = 2 - 3$ lines are shown in Figure 5, including a few cases where the lines overlap IGM absorption lines. Whenever we assessed the blending of the H_2 and IGM lines, we used H_2 lines having line strengths, $f\lambda$, bracketing those of the blended lines (see Table 2)

We estimate a total sight line H_2 column density of $\log N(H_2) \approx 15.71$ in rotational levels $J = 0 - 4$. We find $\log N_J(H_2) = 15.00 \pm 0.30$, 15.48 ± 0.18, 14.76 ± 0.12, 14.73 ± 0.12, and < 14.40 (3σ) for $J = 0, 1, 2, 3,$ and 4, respectively (Table 5). The inferred Doppler parameter is 6 ± 2 $km\,s^{-1}$, and the kinetic temperature derived from the relative populations of the $J = 0, 1$ levels is loosely constrained at $T_{01} \approx 157 \pm 100\,K$. Comparing the H_2 column to the total H I from 21 cm emission yields $f(H_2) = 2N(H_2)/[N(H\ I)+2N(H_2)] \approx 6 \times 10^{-5}$, typical for low-density sight lines through the Milky Way halo (Shull et al. 2000b). For any reasonable values of $N(CO)/N(H_2)$, the CO (A–X) bands in the *HST* bandpass will not be observable. Thus, the primary source of information about molecular gas along the sight line is the H_2 absorption in the *FUSE* bandpass.

6. Discussion

6.1. Intergalactic Medium

A long-standing goal of cosmology is to make an accurate assessment of the amount of baryonic material in the Universe. Using *HST*, it has been possible to survey H I Lyα absorption along numerous sight lines. The 3C 273 sight line is one of the best studied directions. Although most of the Lyα absorbers are weak ($\log N(H\ I) < 14$), several absorbers have higher H I column densities, and the detection of O VI in two systems ($z = 0.00338, 0.12007$) implies very large values of $N(H^+)/N(H\ I)$. Standard photoionization models of low-z clouds also suggest that a significant fraction of the baryonic material may be contained in the form of ionized gas at low redshift (e.g., Shull, Penton, & Stocke 1999). Determining whether the gas is photoionized or collisionally ionized remains an outstanding problem (see, e.g., Savage et al. 2001a).

Our *FUSE* observations of Lyβ absorption in 8 of the IGM clouds yield refined column densities and Doppler parameters for these absorbers (Table 4). Previous column density estimates based on Lyα profile fitting generally produced reliable results for the weak absorbers along the sight line. However, the column density of the 1590 $km\,s^{-1}$ Virgo absorber measured previously was underestimated because the absorption has a considerably smaller Doppler parameter than inferred from the profile fitting. For the 8 absorbers, we find $\langle b \rangle = 25 \pm 10$ $km\,s^{-1}$ with a full spread of $16 \lesssim b(km\,s^{-1}) \lesssim 46$. This range of Doppler parameters is similar to that inferred from the Lyα/Lyβ ratios for stronger Lyα forest absorbers along low-redshift sight lines (Shull et al. 2000a) and at redshifts of 2.0–2.5 (Rauch et al. 1993). For the best constrained case of the 1590 $km\,s^{-1}$ Virgo absorber, the b-value of 16.1 $km\,s^{-1}$ implies $T \lesssim 15,000$ K. This temperature is likely to be even smaller if multiple absorption components are present in the profile as expected (see §4.1).

For the intergalactic path to 3C 273, we expect to find $\sim 1 \pm 1$ O VI absorber with $W_r \gtrsim 30$ mÅ after accounting for line blocking and assuming $dN/dz \approx 15$ (Tripp, Savage, & Jenkins 2000; Savage et al. 2001a). We find at least one, and probably two, O VI absorbers along the sight line. The $z = 0.12007$ absorber has been confirmed by Williger et al. (2001) with STIS data.

The O VI absorption may trace the hot $(T > 10^5 \, \mathrm{K})$ remnants of hierarchical galaxy formation in the presence of cold dark matter as predicted by N-body simulations (e.g., Cen & Ostriker 1999; Davé et al. 1999). Although there has yet been no direct confirmation that any of the O VI absorbers are collisionally ionized plasmas at high temperatures, there are some excellent cases that favor collisional ionization over photoionization unless the absorbers have very low densities $(n < 10^{-5} \, \mathrm{cm}^{-3})$ and large sizes $(L > 100 \, \mathrm{kpc})$ (e.g., Tripp et al. 2001; Savage et al. 2001a). Alternate hypotheses for the origin of the O VI absorption include dynamical heating of gases in groups of galaxies or expulsion of interstellar material by starbursts (e.g., Heckman et al. 2001). There is no prominent group of galaxies at the redshift of the $z = 0.12007$ absorber, and the closest known galaxy has a sufficiently large impact parameter (~ 2.5 Mpc assuming $\mathrm{H_0} = 65 \, \mathrm{km \, s}^{-1}$ Mpc^{-1}; Morris et al. 1993; McLin et al. 2001) that expelled material is unlikely to be a source for the absorption.

The Virgo Cluster is a potential source for the weak O VI absorption associated with the $z = 0.00338$ absorber. Extreme ultraviolet observations of Virgo suggest that the cluster contains a gaseous component with temperatures of $(0.5 - 1.0) \times 10^6 \, \mathrm{K}$ (Lieu et al. 1996; Bonamente, Lieu, & Mittaz 2001), but an upper limit on the amount of O VI emission observed by $FUSE$ (Dixon et al. 2001a) casts doubt upon the widespread existence of a strongly-emitting intracluster medium with $T < 10^6 \, \mathrm{K}$. Our absorption-line measurements are orders of magnitude more sensitive to $10^5 - 10^6 \, \mathrm{K}$ gas than these emission measurements, but the 3C 273 sight line lies well off the center of the cluster, where the amount of extreme ultraviolet emission and hot gas observed at X-ray energies above ~ 2 keV is greatest (see Forman & Jones 1982). However, there are lower levels of X-ray emission in other regions of the cluster (Forman et al. 1979), so it is nonetheless possible that the weak O VI absorption toward 3C 273 at $z = 0.00338$ is related to hot gas within the cluster. The preferred Doppler width of the H I profile for the absorber derived from the curve of growth suggests a temperature of $\lesssim 55,000$ K; this value rises to $\lesssim 100,000$ K (3σ) if the error estimates on $b(\mathrm{H \, I})$ are included in the limit. In either case, it is likely that the absorber has a multi-phase structure if it is collisionally ionized.

X-ray absorption-line observations of O VII and O VIII toward 3C 273 may prove useful for determining whether the O VI absorption traces hot $(10^5 - 10^6 \, \mathrm{K})$, collisionally ionized gas or warm $(10^4 - 10^5 \, \mathrm{K})$ photoionized gas. Unfortunately, the column densities of these species would need to be very large (log N > 16-17) to be studied spectroscopically with the $Chandra$ observatory. The most effective method currently available for studying the low-redshift IGM is ultraviolet absorption-line spectroscopy. Further absorption-line observations of other low-redshift quasars with $FUSE$ and STIS will help to quantify the redshift distribution of the O VI absorbers and their relationship to the IGM Lyα clouds and galaxies.

6.2. The Hot Interstellar Medium

The interstellar O VI absorption toward 3C 273 provides new information about the physical processes governing the production of hot gas along the sight line. Of all the high ions accessible in the ultraviolet spectral region, O VI is the best diagnostic of hot $(T \sim 10^5 - 10^6$ K), collisionally ionized gas since its abundance in the Milky Way ISM is unaffected by photoionization (IP$_{O\,V}$ = 114 eV). O VI has been observed along numerous sight lines in the Milky Way and Magellanic Clouds (Jenkins 1978; Savage et al. 2000, 2001b; Howk et al. 2001b), but the relationship of the hot gas absorption to the absorption traced by other species (e.g., C IV, N V, and low ions) has not yet been studied in detail.

We list the integrated ratios of O VI to N V, C IV, and Si IV for five sight lines in Table 7. The ratios N(O VI)/N(N V) and N(O VI)/N(Si IV) vary by factors of $\sim 2 - 3$ in the sample. N(O VI)/N(C IV) is similar along four of the five sight lines (3C 273, Mrk 509, PKS 2155-304, and H 1821+643) but is a factor of ≈ 3 lower toward ESO 141-G55. Unlike the other sight lines, the ESO 141-G55 sight line passes through the inner regions of the Galaxy, which may account for some of the difference in N(O VI)/N(C IV). Spitzer (1996) noted that the N(O VI)/N(C IV) ratio along 6 halo and 5 disk sight lines observed with *Copernicus* changed from an average value of ~ 6.8 in the disk to ~ 1.1 in the halo. The ionized gas sampled by the extended sight lines listed in Table 7 probably resides primarily in the low halo rather than in the disk.

The constancy of N(O VI)/N(C IV) as a function of velocity along the 3C 273 sight line strongly suggests that the two ions are located in similar regions and are produced by similar processes. Models of turbulent mixing layers (TMLs) having post-mixed gas temperatures of $\sim (2-5) \times 10^5$ K and hot gas entrainment velocities of $\sim 25-100$ km s^{-1} produce more C IV than O VI, typically with N(O VI)/N(C IV) ~ 0.1–0.8 (Slavin, Shull, & Begelman 1993). Over the same temperature range, time-averaged values of N(O VI)/N(C IV) in non-equilibrium radiatively cooling gas are typically $\sim 7 - 14$ (Edgar & Chevalier 1986). Similarly, models that follow the evolution of supernova remnants yield time-averaged values of $\sim 5 - 10$ (Slavin & Cox 1992). In very late stages of evolution ($t \gtrsim 1.3 \times 10^7$ years), the ratio may fall below 2, but generally it is much higher (Shelton 1998). The N(O VI)/N(N V) ratio is typically $\gtrsim 5 - 10$ in both types of cooling, but can drop to lower values in the hotter TMLs. Thus, the interpretation of the observed ratios toward 3C 273 and the other objects listed in Table 7 requires a combination of physical processes to produce the high ions (see, e.g., Shull & Slavin 1994).

Sembach et al. (1997) proposed a hybrid model for the hot gas in the Loop IV region of the sky to explain the observed high ion ratios along several sight lines, including 3C 273; the 3C 273 sight line passes near the edge of the radio continuum emission and X-ray enhancements associated with the North Polar Spur. They suggested that the high ion absorption occurs within a highly fragmented medium within the Loop IV remnant or in the outer cavity walls of the remnant. A similar interpretation was suggested by Heckman et al. (2001) for the outflowing material in the starburst galaxy NGC 1705. Our observations of 3C 273 are consistent with this interpretation

and lend additional support for multiple types of gas along the sight line. In particular, the high velocity absorption wing observed only in O VI (§5.2.2) indicates that there is hot gas at substantially different velocities than the bulk of the material along the sight line.

High velocity O VI is seen along many sight lines through the Milky Way, but in most cases the O VI absorption can be associated with lower ionization stages and appears to be more tightly confined in velocity than the absorption wing toward 3C 273 (e.g., Sembach et al. 2000b; Heckman et al. 2001). Broad wings on O VI profiles are seen along several other sight lines (Savage et al. 2001b), but the detection toward 3C 273 is the only one for which additional information for other highly ionized species is presently available. The high velocity O VI has $N(\text{O VI})/N(\text{C IV}) > 5.1$, which is consistent with the expectations for radiatively cooling gas in fountain flows or young supernova remnants. Furthermore, the ratios of O VI to N V and C IV are also consistent with the values recently determined by Hoopes et al. (2001) for a young remnant in the Small Magellanic Cloud [$N(\text{O VI})/N(\text{N V}) = 17.8 \pm 3.1$ and $N(\text{O VI})/N(\text{C IV}) = 7.9 \pm 0.8$], providing support for the origin of the O VI in a supernova remnant region.

The broad O VI positive velocity absorption wing toward 3C 273 is probably the manifestation of hot gas being vented out of the Galactic disk into the halo. The outflow of hot ($T \sim 10^6$ K) gas is expected in regions where there are multiple supernova explosions; the "chimneys" serve as conduits for the hot gas that may eventually return to the Galactic disk as cool high velocity clouds (e.g., Shapiro & Field 1976; Bregman 1980; Norman & Ikeuchi 1989). In the direction of 3C 273, there are clear signatures that multiple energetic events in the disk have produced hot gas. Radio Loop I is filled with X-ray emission (Snowden et al. 1995), Loop IV was probably created by the events that reheated Loop I (Iwan 1980), and the North Polar Spur is prominent in X-ray emission (Snowden et al. 1995). Alternatively, the high velocity wing may trace the tidal debris wakes of HVCs moving through the Galactic halo or the remnants of infalling or tidally disturbed galaxies (e.g., the Sagittarius dwarf or Magellanic Stream). Until additional information can be obtained that would provide support for the debris hypothesis, we favor the former interpretation as the most likely source of the high velocity O VI.

6.3. Limits on Interstellar O VI Emission

Dixon et al. (2001b) have recently reported a serendipitous detection of O VI emission from the diffuse ISM of the Milky Way in the direction of the Virgo Cluster. Observing with the LWRS apertures on *FUSE* for 11 ksec, they found an interstellar O VI $\lambda 1031.926$ photon surface brightness of 2900 ± 700 ph cm^{-2} s^{-1} sr^{-1} and an intrinsic line width of < 80 km s^{-1} (FWHM) toward M 87 in the direction $l = 284.1°, b = +74.5°$. Such a result may be fortuitous, since the inferred O VI column density they derived from a low S/N absorption-line spectrum of the nucleus of M 87 is only $(1.4 \pm 0.8) \times 10^{14}$ cm^{-2}, which is a factor of 4 less than the value of $(5.4 \pm 0.5) \times 10^{14}$ cm^{-2} we measure toward 3C 273 (about 10.3° away) and a factor of ~ 2 less than the high-latitude sight line toward NGC 5548 ($l = 32.0°, b = +70.5°$; Savage et al. 2001b). Furthermore, Shelton et al.

(2001) required nearly 200 ksec of integration time with the same *FUSE* LWRS apertures to detect diffuse emission at a level of 2930 ± 700 ph cm^{-2} s^{-1} sr^{-1} in the direction $l = 315.0°, b = -43.1°$. In this latter case, it is possible that a nearby interstellar cloud obscures much of the emission from material beyond a few hundred parsecs.

During our absorption-line observation of 3C 273 through the LWRS apertures, we also observed nearby regions of sky in the MDRS ($4'' \times 20''$) apertures. The LWRS and MDRS apertures are separated by an angle of approximately $3.5'$ on the sky and have a size ratio of 11.25. The MDRS aperture provides a filled-slit spectral resolution of ≈ 0.1 Å (≈ 30 km s^{-1}). In Figure 10 we show a portion of the MDRS data for the LiF1 channel, processed and extracted in the same manner as the LWRS data. The dashed line in the figure shows an emission line having a surface brightness of 15,000 ph cm^{-2} s^{-1} sr^{-1} and a width the same as that of the absorption toward 3C 273 (FWHM ≈ 120 km s^{-1} – see §5.1). The two thick solid curves overplotted on the data are the profiles expected for O VI emission having FWHM = 80 km s^{-1} and photon surface brightnesses of 3000 and 15,000 ph cm^{-2} s^{-1} sr^{-1}, comparable to and a factor of 5 greater, respectively, than the emission observed by Dixon et al. (2001b) toward M 87. The 3σ upper limit of 15,000 ph cm^{-2} s^{-1} sr^{-1} set by the 3C 273 data corresponds to an integrated line flux of 5.4×10^{-16} erg cm^{-2} s^{-1} through the MDRS aperture.

We cannot rule out O VI emission at the level observed by Dixon et al. toward M 87, but we find that the factor of 4–5 larger O VI column density for the 3C 273 sight line does not likely have a corresponding factor of 5 larger surface brightness of O VI emission. The limit for the 3C 273 sight line is less than the level of diffuse interstellar O VI emission ($\sim 36,000 \pm 17,000$ ph cm^{-2} s^{-1} sr^{-1}) reported by Dixon, Davidsen, & Ferguson (1996) toward NGC 4038 in the direction $l = 287.0°, b = +42.5°$, about 21° from 3C 273. The observed differences in O VI emission strength along the 3C 273, M 87, and NGC 4038 sight lines may result from differences in the temperatures of the O VI-emitting gases in the three directions. 3C 273 lies near an X-ray bright region of the North Polar Spur, whereas M 87 lies in a region of slightly lower soft (1/4 keV) X-ray brightness, and NGC 4038 is in a direction of much lower soft X-ray emission (Snowden et al. 1995).

A primary problem with interpreting the presence or absence of O VI emission along a sight line is the unknown geometry of the emitting gas and its relationship to the absorbing gas. Until now, this problem has been confounded by the additional uncertainties incurred when measuring emission and absorption along different sight lines separated by several degrees or more on the sky (see, e.g., Dixon et al. 1996). The 3σ limit for the ratio of O VI $\lambda 1031.926$ surface brightness (in energy units) to O VI column density toward 3C 273 is $I_{\lambda 1032} / N(\text{O VI}) < 5.4 \times 10^{-22}$ erg s^{-1} sr^{-1}, under the standard assumption that the O VI absorption and emission arise in the same gas.[11] This can be compared to a value of $(4.0 \pm 2.5) \times 10^{-22}$ erg s^{-1} sr^{-1} toward M 87 using measures of $I_{\lambda 1032}$ and N(O VI) from Dixon et al. (2001b).

---

[11]Note that 1031.926 Å photons have energies of 1.925×10^{-11} erg.

Following Shull & Slavin (1994, see their Eq. 5), we express the electron density in terms of the observable quantities and the electron-impact excitation rate coefficient, $\langle \sigma v \rangle_e$, to write

$$n_e = \frac{3}{2} \frac{4\pi}{\langle \sigma v \rangle_e} \frac{I_{1032}}{N(O\ VI)} = 2.28 \times 10^{17} \exp\left[\frac{1.392 \times 10^5\ K}{T}\right] \frac{T^{1/2}}{\bar{\Omega}(T)} \frac{I_{1032}}{N(O\ VI)} \tag{7}$$

where $\bar{\Omega}(T)$ is the Maxwellian-averaged collision strength for de-excitation of the O VI doublet. The factor of 3/2 accounts for the conversion of doublet quantities to values appropriate for the 1032 Å line, and the ratio $I_{\lambda 1032}/N(O\ VI)$ has units of erg s^{-1} sr^{-1}. For $T = 2 \times 10^5$ K and $T = 5 \times 10^5$ K, $\bar{\Omega}(T) = 5.65$ and 6.31, respectively (see Shull & Slavin 1994). Over this temperature range, we find $n_e \lesssim 0.02$ cm^{-3}, which yields a limit on the thermal pressure P/k $= 1.92 n_e T \lesssim 7700$ cm^{-3} K for $T \approx 2 \times 10^5$ K and $\lesssim 19,200$ cm^{-3} K for $T \approx 5 \times 10^5$ K, assuming a fully ionized gas and $n_{He}/n_H = 0.1$. Note that if the absorption and emission do not arise in the same gas, these limits would increase if foreground material absorbs the emitted O VI photons.

Time-dependent ionization models should be used to compute the ratio $I_{\lambda 1032}/N(O\ VI)$. Predicted time-averaged values of $I_{\lambda 1032}/N(O\ VI)$ in units of 10^{-22} erg s^{-1} sr^{-1} range from $\sim 2.0 - 2.2$ for turbulent mixing layers with post-mixed gas temperatures of $\sim (2-5) \times 10^5$ K (Slavin et al. 1993) to ~ 10 for conductive interfaces (Borkowski, Balbus, & Fristrom 1990). A hot fountain flow with a mass flux of ~ 4 M$_\odot$ yr^{-1} to either side of the Galactic plane is predicted to have a value of $\sim 1.3 - 3.4$, depending upon whether the cooling is isochoric or isobaric (Edgar & Chevalier 1986). However, alternate cooling flow models predict values in excess of ~ 10 (e.g., Shapiro & Benjamin 1992)[12]. Note that none of these predictions account for the effects of foreground absorption on the observed flux of the emitted O VI photons. A hybrid model of hot gas production involving both turbulent mixing and conduction or radiative cooling of hot ($T \sim 10^6$ K) gas as suggested by Sembach et al. (1997) for the 3C 273 sight line and other directions in the Loop IV region is consistent with the available emission-line data.

6.4. The Warm Ionized Interstellar Medium

The WIM is a fundamental component of the ISM that has been studied primarily through optical emission-line observations of Hα, [S II], and [N II] (see Reynolds 1993). To date, there has been little high quality absorption-line information available to determine the fundamental properties of the WIM other than a study of the Al III scale height ($h_{Al\ III} \sim h_{e-} \sim 1$ kpc; Savage et al. 1990) and a study of the WIM dust composition derived from S III and Al III observations for several sight lines (Howk & Savage 1999). This latter study found that that the degree of grain destruction in the WIM is comparable to that in the warm neutral medium (see Sembach & Savage 1996). Our observations of S III and Fe II-III toward 3C 273 confirm this result.

---

[12] The factor of ~ 10 difference compared to the Edgar & Chevalier (1986) models arises from the different densities assumed for the cooling gas (10^{-2} vs. 10^{-3} cm^{-3}).

The great breadth of the interstellar C III absorption toward 3C 273 indicates that the moderately ionized interstellar gas has a velocity extent comparable to or slightly greater than that of the neutral gas. Beyond ~ -100 km s^{-1}, N(C III)/N(C II) > 1 and N(C III)/N(C IV) $\gtrsim$ 3, conditions that are not both satisfied for neutral or diffuse photoionized regions but are met for post-shocked regions (see Shull & McKee 1979).

The amount of S III relative to S II observed toward 3C 273 is not compatible with production in a purely photoionized WIM of the type described by Sembach et al. (2000a). The requirement for other sources of ionization is not surprising given the large amount of highly ionized gas observed along the sight line. Comparison of the 3C 273 WIM results to similar measurements for halo sight lines that do not pass through supernova remnants or other known sources of hot gas would help to characterize the general relationship of the hot and warm ionized components of the ISM. A study of the optical line emission in the immediate vicinity of the 3C 273 sight line may also help to quantify the contributions of the various high ion production mechanisms to the S III absorption.

7. Summary

We have observed the ultraviolet-bright quasar 3C 273 to study the intergalactic and interstellar absorption along the sight line. We briefly summarize the primary results of this investigation as follows:

1) We searched for Lyβ and metal-line (C III, O VI) absorption in the 8 known IGM Lyα absorbers along the sight line having W_r(Lyα) > 50 mÅ. The detections of Lyβ confirm the identifications of the Lyα lines and provide refined estimates of the H I column densities and Doppler parameters of the clouds. We find a range of Doppler parameters, $b \approx 16 - 46$ km s^{-1}.

2) We detect O VI absorption in the 1015 km s^{-1} Virgo absorber at the $2 - 3\sigma$ level. This is the lowest redshift IGM O VI absorber identified outside the Local Group. The O VI absorption may be associated with hot, X-ray emitting gas in the cluster. However, the Doppler width of the H I absorption suggests that cooler gas ($T \lesssim 10^5$ K) is also present.

3) Multiple Lyman series H I lines (Lyβ–Lyθ) in addition to Lyα are detected in the 1590 km s^{-1} Virgo absorber. We revise the previous H I column density estimate obtained by Lyα profile fitting upward by a factor of ~ 43 to $\log N$(H I) $= 15.85^{+0.10}_{-0.08}$. *This absorber is now known to contain ten times more H I than all of the other absorbers along the sight line combined.* The Doppler parameter decreased from a value of ~ 34 km s^{-1} to a value of ~ 16 km s^{-1}. This line width implies $T \leq 15,000$ K. Using a limit on the amount of C III present, we find N(H$^+$)/N(H I) $< 4.5 Z^{-1}$. This absorber may contain multiple components.

4) We detect C III and O VI in the absorber at $z = 0.12007$. The O VI absorption is weak [W_λ(O VI 1031) ≈ 30 mÅ]. This absorber is predominantly ionized and has N(H I)/N(O VI) $\approx 1.7^{+0.6}_{-0.8}$, corresponding to N(H$^+$)/N(H I) $\geq 4000 Z^{-1}$. Other absorbers along the sight line have

limits on N(H I)/N(O VI) ranging from > 0.5 ($z = 0.04898$) to > 148 ($z = 0.00530$). Approximately 1 ± 1 O VI absorber with $W_r \gtrsim 50$ mÅ is expected for the sight line given current estimates of the number density of O VI absorbers at low redshift.

5) We analyzed high-resolution (Ech-A) GHRS observations of the Lyα absorption at $z = 0.02947$. The absorber is optically thin and appears to consist of a combination of broad ($b \sim 50$ km s^{-1}) and narrow ($b \sim 25$ km s^{-1}) components. If thermal broadening dominates the former, the temperature of the gas may exceed $\sim 10^5$ K.

6) We measured strong interstellar O VI in the direction of 3C 273. The main absorption spans a velocity range from -100 to $+100$ km s^{-1}. The O VI, N V, and C IV lines have very similar shapes, with roughly constant ratios across the -100 to $+100$ km s^{-1} velocity range. There is an enhancement in the ratio of Si IV to the other high ions at positive velocities where low ionization and molecular gas is observed. Much of the interstellar high ion absorption toward 3C 273 probably occurs within a highly fragmented medium within the Loop IV remnant or in the outer cavity walls of the remnant. Multiple ionization mechanisms are required.

7) We place a flux limit of 5.4×10^{-16} erg cm^{-2} s^{-1} on the amount of O VI emission present in the LiF1 MDRS aperture. Assuming that the O VI emission and absorption along the sight line occur within the same gas, we find $n_e \lesssim 0.02$ cm^{-3} and a thermal pressure P/k $\lesssim 11,500$ cm^{-3} K for a temperature of 3×10^5 K.

8) An additional high velocity wing of O VI absorption containing about 13% of the total O VI is present at velocities between $+100$ and $+240$ km s^{-1}. This absorption wing is not observed in other species, but similar O VI wings have been observed along other sight lines through the Galactic halo. The broad O VI absorption wing may trace the expulsion of hot gas out of the Galactic disk into the halo.

9) The neutral and low ionization ISM along the sight line occurs within two groups of clouds centered on LSR velocities of ~ -15 and $\sim +23$ km s^{-1}. The negative velocity group contains most of the H I gas. Abundance estimates for the interstellar clouds are similar to those for other halo clouds. The warm neutral and warm ionized clouds along the sight line have similar dust-phase abundances, implying that the properties of the dust grains in the two types of clouds are similar.

10) Interstellar H$_2$ absorption is present along the 3C 273 sight line at a level of $\log N(\text{H}_2) \sim 15.71$. The H$_2$ is associated with the neutral and low ionization gas at positive velocities. The H$_2$ does not trace the main column density concentration along the sight line observed in H I 21 cm emission.

REFERENCES

Abgrall, H., Roueff, E., Launay, F., Roncin, J.Y., & Subtil, J.L. 1993a, A&AS, 101, 273

Abgrall, H., Roueff, E., Launay, F., Roncin, J.Y., & Subtil, J.L. 1993b, A&AS, 101, 323

Anders, E., & Grevesse, N. 1989, Geochim. Cosmochim. Acta, 53, 197

Bahcall, J.N., Bergeron, J., Boksenberg, A., et al. 1993, ApJS, 87, 1

Bahcall, J.N., Januzzi, B.T., Schneider, D.P., Hartig, G.F., Bohlin, R., & Junkkarinen, V. 1991, ApJ, 377, L5

Berkhuijsen, E., Haslam, C.G.T., & Salter, C.J. 1971, A&A, 14, 252

Bonamente, M., Lieu, R., & Mittaz, J.P.D 2001, ApJ, 547, L7

Borkowski, K.J., Balbus, S.A., & Fristrom, C.C. 1990, ApJ, 335, 501

Brandt, J.C., Heap, S.R., Beaver, E.A., et al. 1993, AJ, 105, 831

Brandt, J.C., Heap, S.R., Beaver, E.A., et al. 1997, AJ, 114, 554

Bregman, J.N. 1980, ApJ, 236, 577

Burks, J.S., York, D.G., Blades, J.C., Bohlin, R.C., & Wamsteker, W. 1991, ApJ, 381, 55

Burks, J.S., Bartko, F., Shull, J.M., et al. 1994, ApJ, 437, 630

Cen, R., & Ostriker, J.P. 1999, ApJ, 514, 1

Colomb, F.R., Poppel, W.G.L., & Heiles, C. 1980, A&AS, 40, 47

Davé, R., Hernquist, L., Katz, N., & Weinberg, D.H. 1999, ApJ, 511, 521

Davidsen, A.F. 1993, Science, 259, 327

Dixon, W.V., Davidsen, A.F., & Ferguson, H.C. 1996, ApJ, 465, 288

Dixon, W.V., Sallmen, S., Hurwitz, M., & Lieu, R. 2001a, ApJ, 552, L25

Dixon, W.V., Sallmen, S., Hurwitz, M., & Lieu, R. 2001b, ApJ, 552, L69

Edgar, R.J., & Chevalier, R.A. 1986, ApJ, 310, L27

Forman, W., & Jones, C. 1982, ARA&A, 20, 547

Forman, W., Schwarz, J., Jones, C., Liller, W., & Fabian, A.C. 1979, ApJ, 234, L27

Heiles,C., Chu. Y.-H., Reynolds, R.J., Yegingil, I., & Troland, T.H. 1980, ApJ, 242, 533

Heckman, T.M., Sembach, K.R., Meurer, G.R., Strickland, D.K., Martin, C.L., Calzetti, D., & Leitherer, C. 2001, ApJ, in press (astro-ph/0102283)

Hoopes, C.G., Sembach, K.R., Howk, J.C., & Blair, W.P. 2001, ApJL, submitted

Howk, J.C., & Savage, B.D. 1999, ApJ, 517, 746

Howk, J.C., Savage, B.D., & Fabian, D. 1999, ApJ, 525, 253

Howk, J.C., Sembach, K.R., & Savage, B.D. 2001a, in prep

Howk, J.C., Sembach, K.R., Savage, B.D., Massa, D., Friedman, S.D., & Fullerton, A.W. 2001b, in prep

Hurwitz, M., Appenzeller, I., Barnstedt, J., et al. 1998, ApJ, 500, L61

Iwan, D. 1980, ApJ, 239, 316

Jenkins, E.B. 1978, ApJ, 219, 845

Jenkins, E.B. 1987, In *Interstellar Processes*, eds. D.J. Hollenbach & H.A. Thronson, (Dordrecht: Reidel), 533

Lieu, R., Mittaz, J.P.D., Bowyer, S., Lockman, F., Hwang, C.-Y., & Schmitt, J.H.M.M. 1996, ApJ, 458, L5

Moore, C.E. 1970, Ionization Potentials and Ionization Limits Derived from the Analysis of Optical Spectra (NSRDS-NBS Rep. 34; Washington, D.C: U.S. Dept. of Commerce)

McCammon, D., Burrows, D.N., Sanders, W.T., & Kraushaar, W.L. 1983, ApJ, 269, 107

McLin, K., Stocke, J.T., Weymann, R.J., Penton, S.V., & Shull, J.M. 2001, ApJ, submitted

Mihalas, D. & Binney, J. 1981, *Galactic Astronomy*, 2nd ed., (San Francisco: Freeman), Ch. 6

Moos, H.W., Cash, W.C., Cowie, L.L., et al. 2000, ApJ, 538, L1

Morris, S.L., Weymann, R.J., Dressler, A., et al. 1993, ApJ, 419, 524

Morris, S.L., Weymann, R.J., Savage, B.D., & Gilliland, R.L. 1991, ApJ, 377, L21

Morton, D.C. 1991, ApJS, 77, 119

Norman, C., & Ikeuchi, S. 1989, ApJ, 345, 372

Oegerle, W.R., Tripp, T.M., Sembach, K.R., et al. 2000, ApJ, 538, L23

Penton, S.V., Shull, J.M., & Stocke, J.T. 2000a, ApJ, 544, 150

Penton, S.V., Stocke, J.T., & Shull, J.M. 2000b, ApJS, 130, 121

Penton, S.V., Stocke, J.T., & Shull, J.M. 2001, ApJ, submitted

Rauch, M., Carswell, R.F., Webb, J.K., & Weymann, R.J. 1993, MNRAS, 260, 589

Reynolds, R.J. 1993, in Back to the Galaxy, ed. S. Holt & F. Verter (New York: American Institute of Physics), 156

Richter, P., Savage, B.D., Wakker, B.P., Sembach, K.R., & Kalberla, P.M.W. 2001a, ApJ, in press (astro-ph/0010343)

Richter, P., Sembach, K.R., Wakker, B.P., Savage, B.D., Tripp, T.M., et al. 2001b, in press

Sahnow, D.S., Moos, H.W., Ake, T.B., et al. 2000a, ApJ, 538, L7

Sahnow, D.S., Moos, H.W., Ake, T.B., et al. 2000b, SPIE, 4013, 334

Savage, B.D., Edgar, R.J., & Diplas, A. 1990, ApJ, 361, 107

Savage, B.D., Lu, L., Weymann, R.J., Morris, S.L., & Gilliland, R.L. 1993, ApJ, 404, 124

Savage, B.D., & Sembach, K.R. 1991, ApJ, 379, 245

Savage, B.D., & Sembach, K.R. 1996, ARA&A, 34, 279

Savage, B.D., Sembach, K.R., Jenkins, E.B., et al. 2000, ApJ, 538, L27

Savage, B.D., Sembach, K.R., & Lu, L. 1997, AJ, 113, 2158

Savage, B.D., Sembach, K.R., Tripp, T.M., & Richter, P. 2001a, ApJ, submitted

Savage, B.D., et al. 2001b, in prep

Sembach, K.R. 1999, in the *Proceedings of the Stromlo Workshop on High Velocity Clouds*, eds. B.K. Gibson & M.E. Putnam, ASP Conf. Series (San Francisco: ASP), 243

Sembach, K.R., & Savage, B.D. 1992, ApJS, 83, 147

Sembach, K.R., & Savage, B.D. 1996, ApJ, 457, 211

Sembach, K.R., Howk, J.C., Ryans, R.S.I., & Keenan, F.P. 2000a, ApJ, 528, 310

Sembach, K.R., Howk, J.C., Savage, B.D., & Shull, J.M., 2001, AJ, 121, 992

Sembach, K.R., Savage, B.D., & Hurwitz, M. 1999a, ApJ, 524, 98

Sembach, K.R., Savage, B.D., Lu, L., & Murphy, E.M. 1999b, ApJ, 515, 108

Sembach, K.R., Savage, B.D., Shull, J.M., et al. 2000b, ApJ, 538, L31

Sembach, K.R., Savage, B.D., & Tripp, T.M. 1997, ApJ, 480, 216

Shapiro, P.R., & Benjamin, R.A. 1992, in Star Forming Galaxies and Their Interstellar Media, ed. J.J. Franco (New York: Cambridge University Press)

Shapiro, P.R., & Field, G.B. 1976, ApJ, 205, 762

Shelton, R.L. 1998, ApJ, 504, 785

Shelton, R.L., Kruk, J.W., Murphy, E.M., et al. 2001, ApJ, in press

Shull, J.M., Giroux, M.L., Penton, S.V., et al. 2000a, ApJ, 528, L13

Shull, J.M., & McKee, C.F. 1979, ApJ, 227, 131

Shull, J.M., Penton, S.V., & Stocke, J.T. 1999, PASA, 16, 95

Shull, J.M., & Slavin, J.D. 1994, ApJ, 427, 784

Shull, J.M., Tumlinson, J., Jenkins, E.B., et al. 2000b, ApJ, 528, L73

Slavin, J.D., & Cox, D.P. 1992, ApJ, 392, 131

Slavin, J.D., Shull, J.M., & Begelman, M.C. 1993, ApJ, 407, 83

Sofia, U.J., & Jenkins, E.B. 1998, ApJ, 499, 951

Snowden, S.L., Freyberg, M.J., Plucinsky, P.P., et al. 1995, ApJ, 454, 643

Spitzer, L. 1978, Physical Processes in the Interstellar Medium (Wiley: New York)

Spitzer, L. 1996, ApJ, 458, L29

Sutherland, R.S., & Dopita, M.A. 1993, ApJS, 88, 253

Tammann, G.A. 1972, A&A, 21, 355

Tripp, T.M., Savage, B.D., & Jenkins, E.B. 2000, ApJ, 534, L1

Tripp, T.M., Stocke, J.T., Giroux, M.L., Tumlinson, J., & Oegerle, W.R. 2001, ApJ, submitted

Weymann, R., Rauch, M., Williams, R., Morris, S., & Heap, S. 1995, ApJ, 438, 650

Williger, G., Heap, S.R., Weymann, R., et al. 2001, in prep

York, D.G., Ratcliff, S., Blades, J.C., Wu, C.C., Cowie, L.L., & Morton, D.C. 1984, ApJ, 276, 92
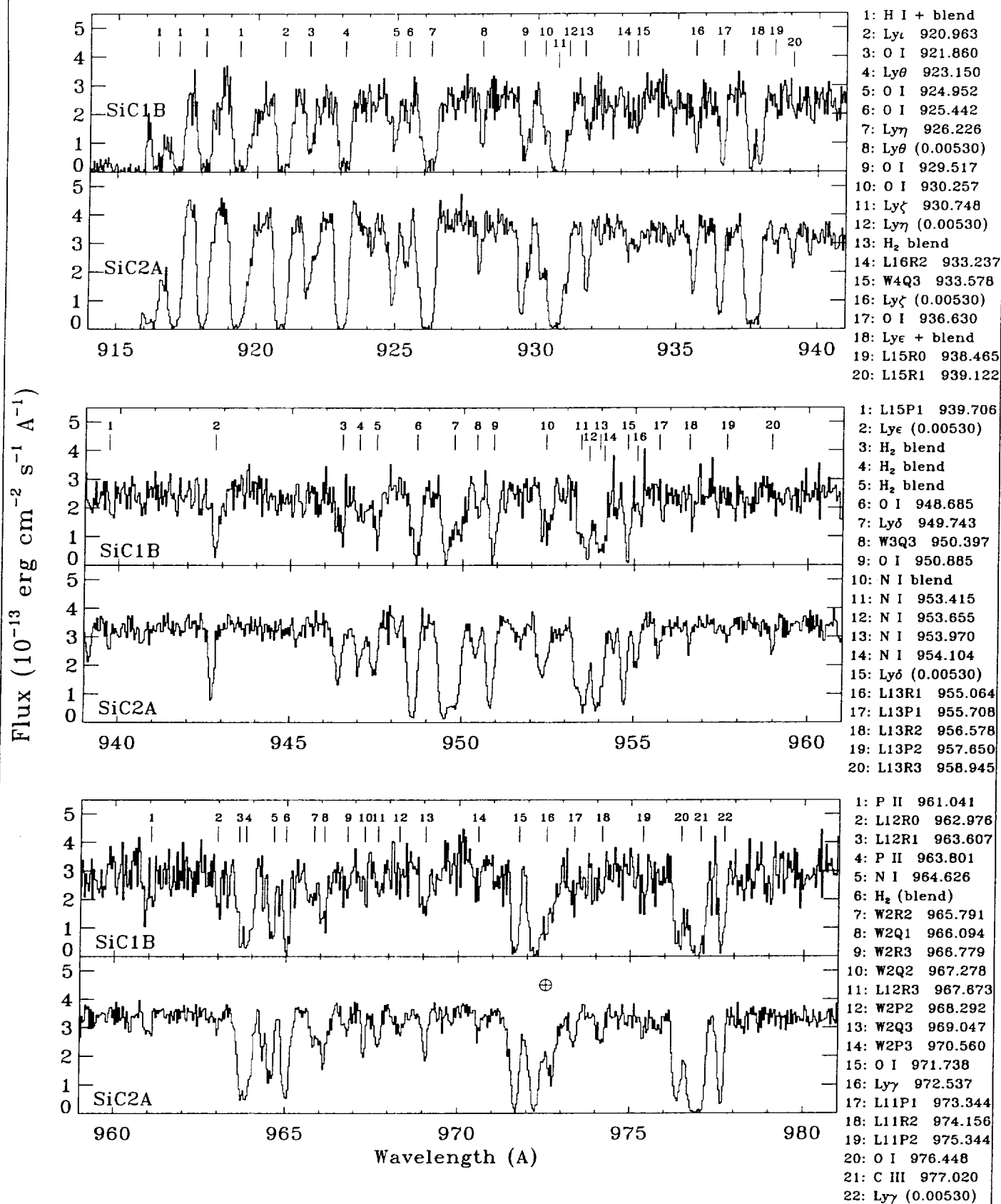
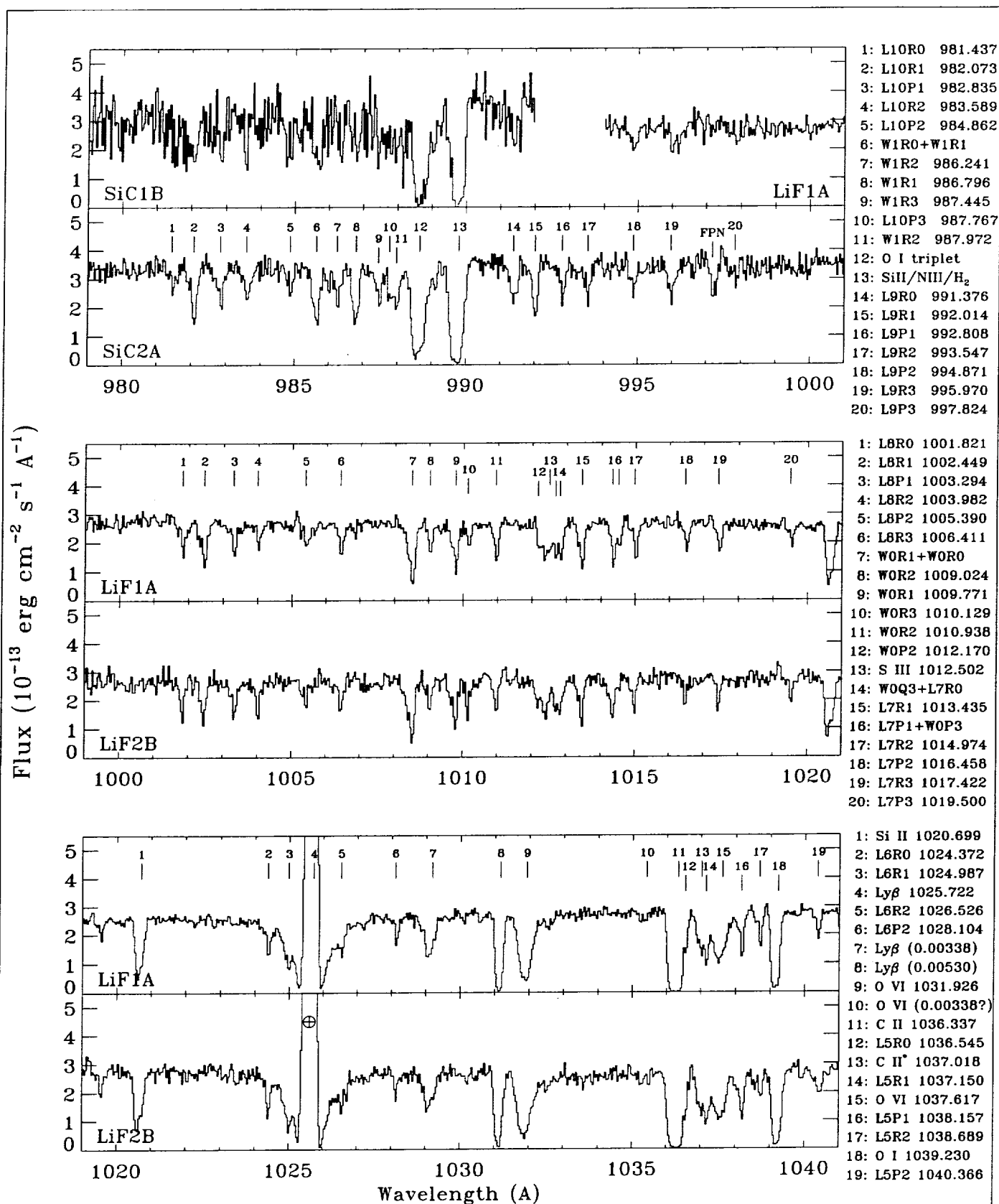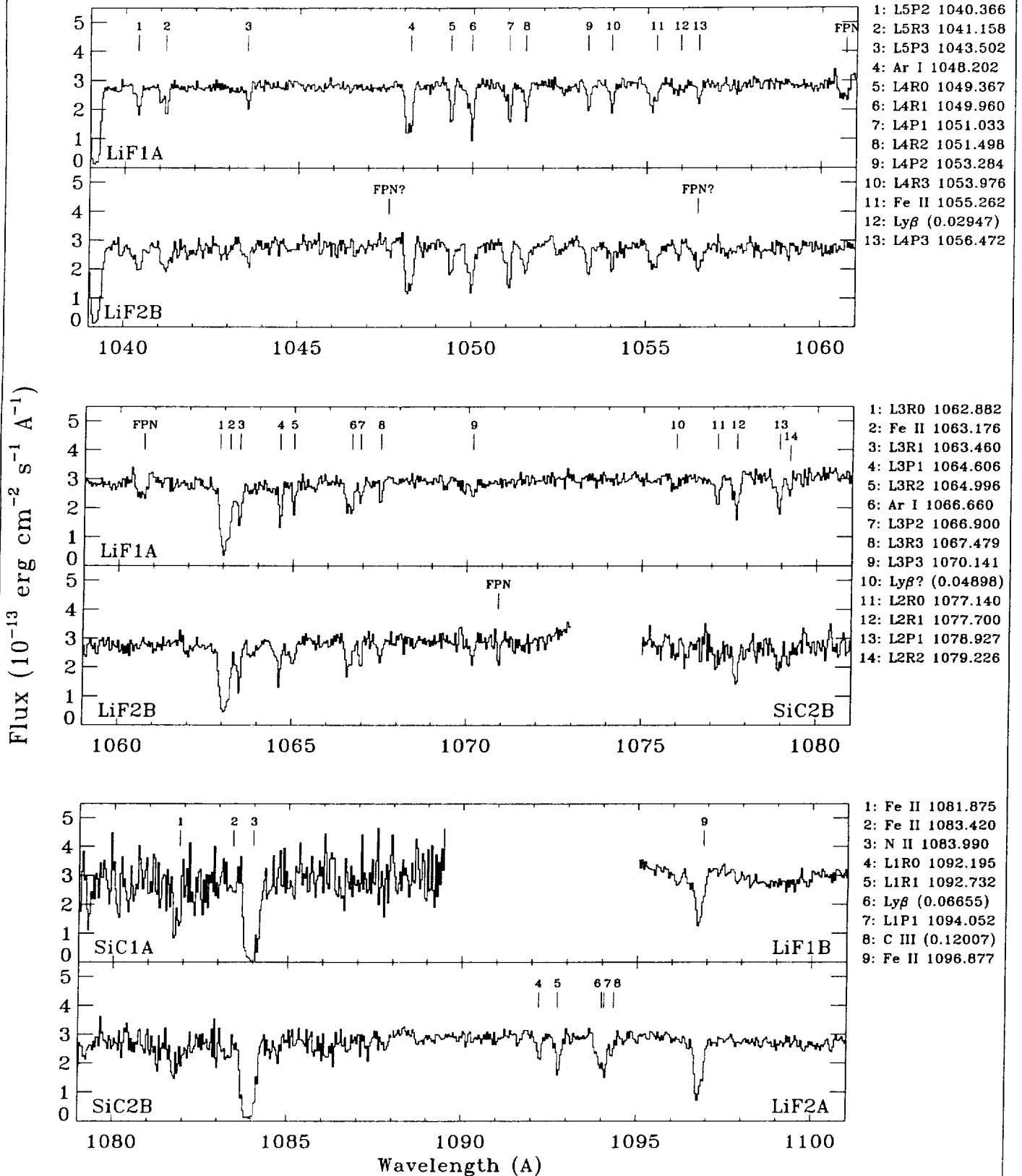Fig. 1.— See caption at end of figure.
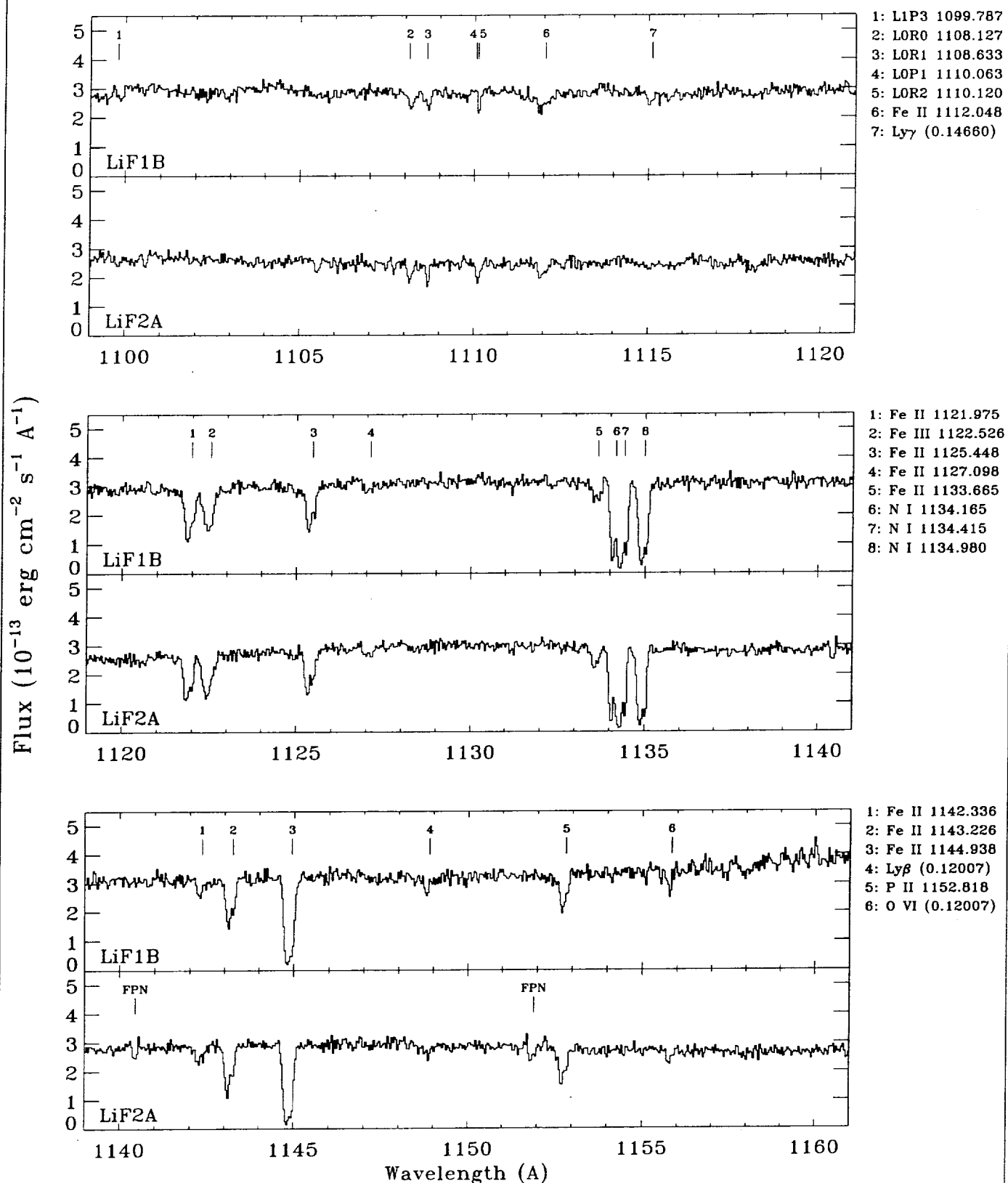
Fig. 1.— (continued)

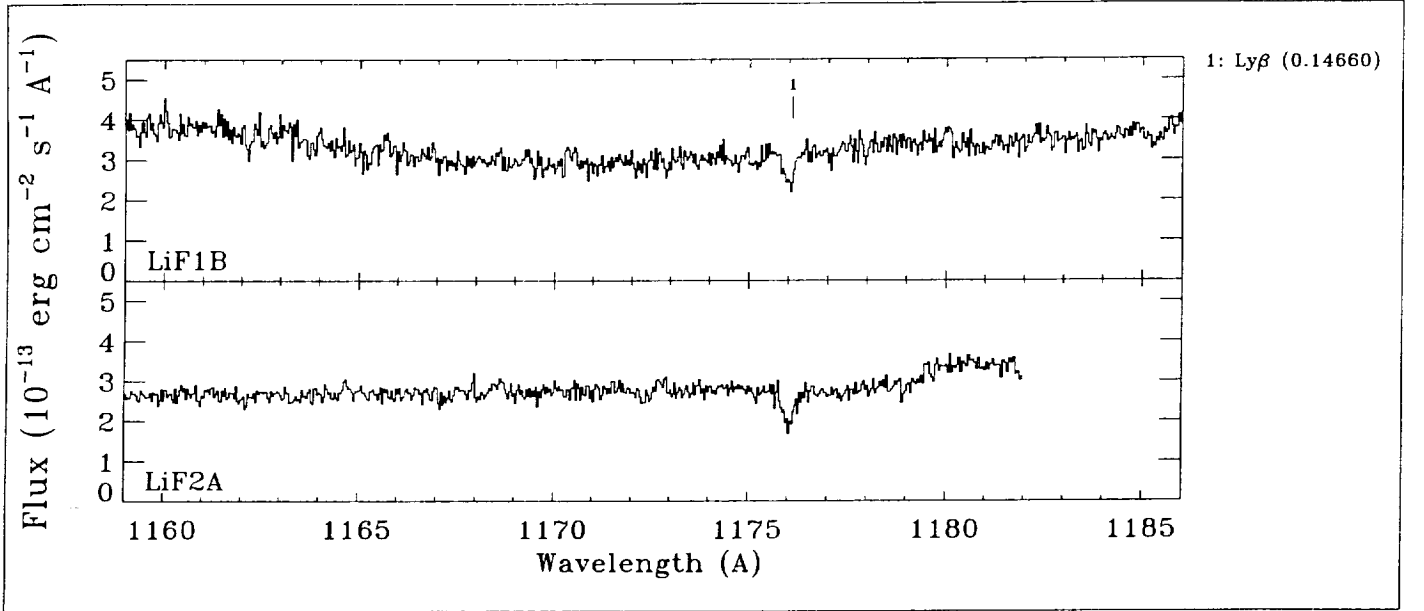Fig. 1.— (continued)

Fig. 1.— (continued)

Fig. 1.— *FUSE* spectra of 3C 273 from 912 to 1186 Å. The data from the most sensitive detector segments are shown at each wavelength (detector #1 on top, detector #2 on bottom). The data have a resolution of approximately 17–22 $km s^{-1}$ (FWHM), depending upon wavelength and detector segment. The spectra shown have been binned into 0.038 Å samples and have $S/N \approx$ 20–35 per resolution element. (This binning is larger than the binning used in the analyses described in the text). Prominent interstellar and intergalactic lines are identified to the right of each panel. Molecular lines are identified by their band (Werner or Lyman), upper vibrational level (1-16), and rotational transition (R, P, or Q with lower rotational state $J = 1 - 3$). Numerous additional weak lines are present but are not indicated for clarity. Several features resulting from fixed-pattern noise introduced by the *FUSE* detectors are indicated with "FPN" above the spectra.
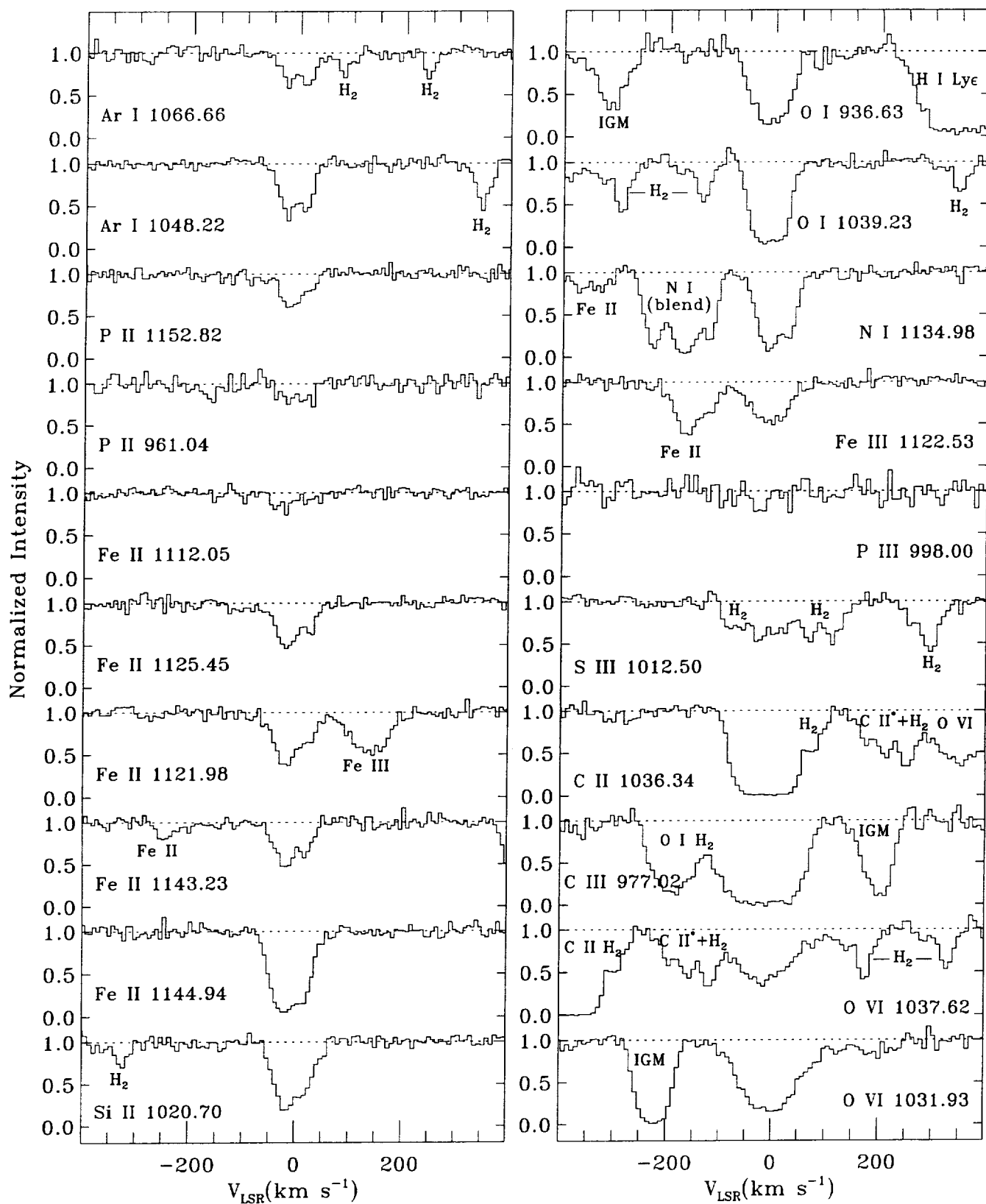
Fig. 2.— (See caption on next page.)

Figure 2.– Continuum-normalized interstellar absorption profiles observed by $FUSE$ along the the 3C 273 sight line (single channel data). The primary absorption features are indicated by ion and wavelength below each spectrum. Additional features appearing in the velocity range shown are labeled immediately above or below the primary absorption feature. In a few cases, redshifted Lyβ absorption lines of intervening IGM clouds are present. Note the broad shallow wing on the O VI $\lambda1031.926$ line at velocities $+100 \leq v_{LSR} \leq +240$ km s^{-1}.
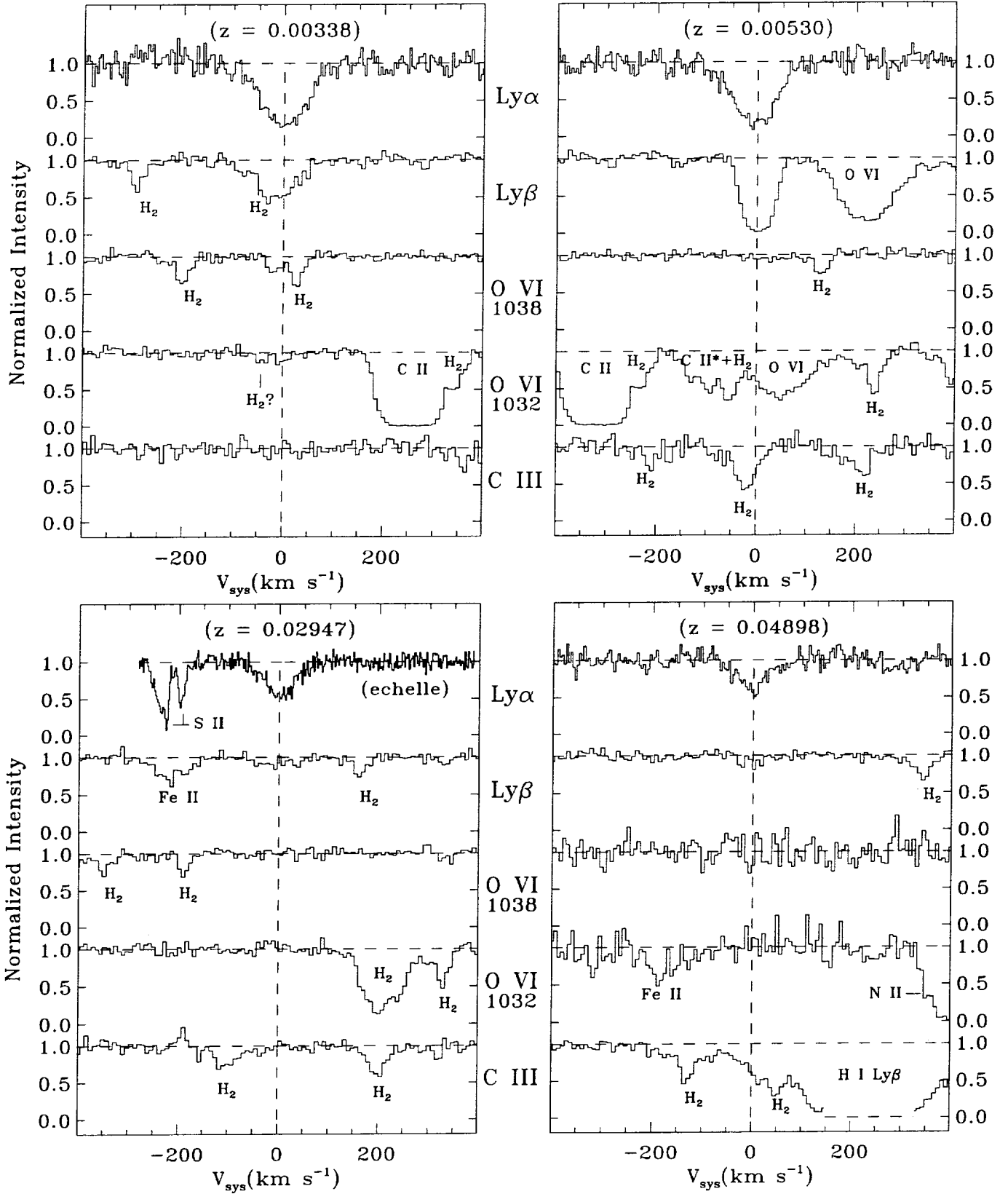
Fig. 3.— See caption at end of figure.
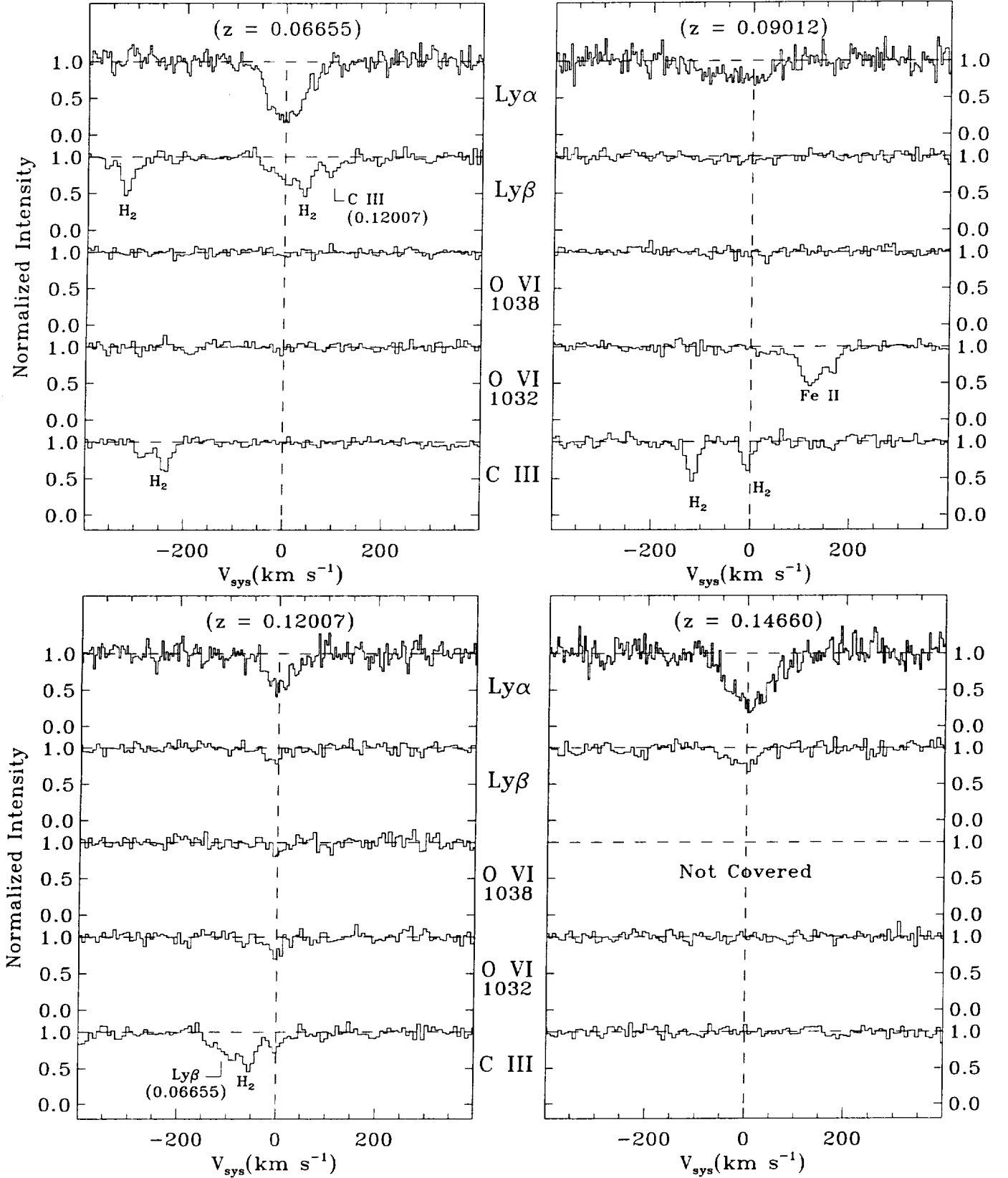
Fig. 3.— (continued)

Fig. 3.– Continuum-normalized Lyα, Lyβ, O VI λ1037.617, O VI λ1031.926, and C III λ977.020 absorption profiles for eight of the previously identified Lyα absorbers along the 3C 273 sight line as a function of rest frame velocity. Only data from one channel is shown for each line observed by *FUSE*. The redshift of the absorption is indicated at the top of each panel. The Lyα profiles are pre-COSTAR GHRS data except for the $z = 0.02947$ system, for which GHRS echelle (FWHM $\approx$ 3.5 km s^{-1}) data were available. Lyβ absorption is detected for each system. O VI absorption is detected in the $z = 0.00338$ and $z = 0.12007$ absorbers. C III absorption is detected only in the $z = 0.12007$ absorber. The O VI λ1037.617 line in the $z = 0.14660$ absorber was not covered by the *FUSE* bandpass. Galactic lines are identified immediately above or below each spectrum.
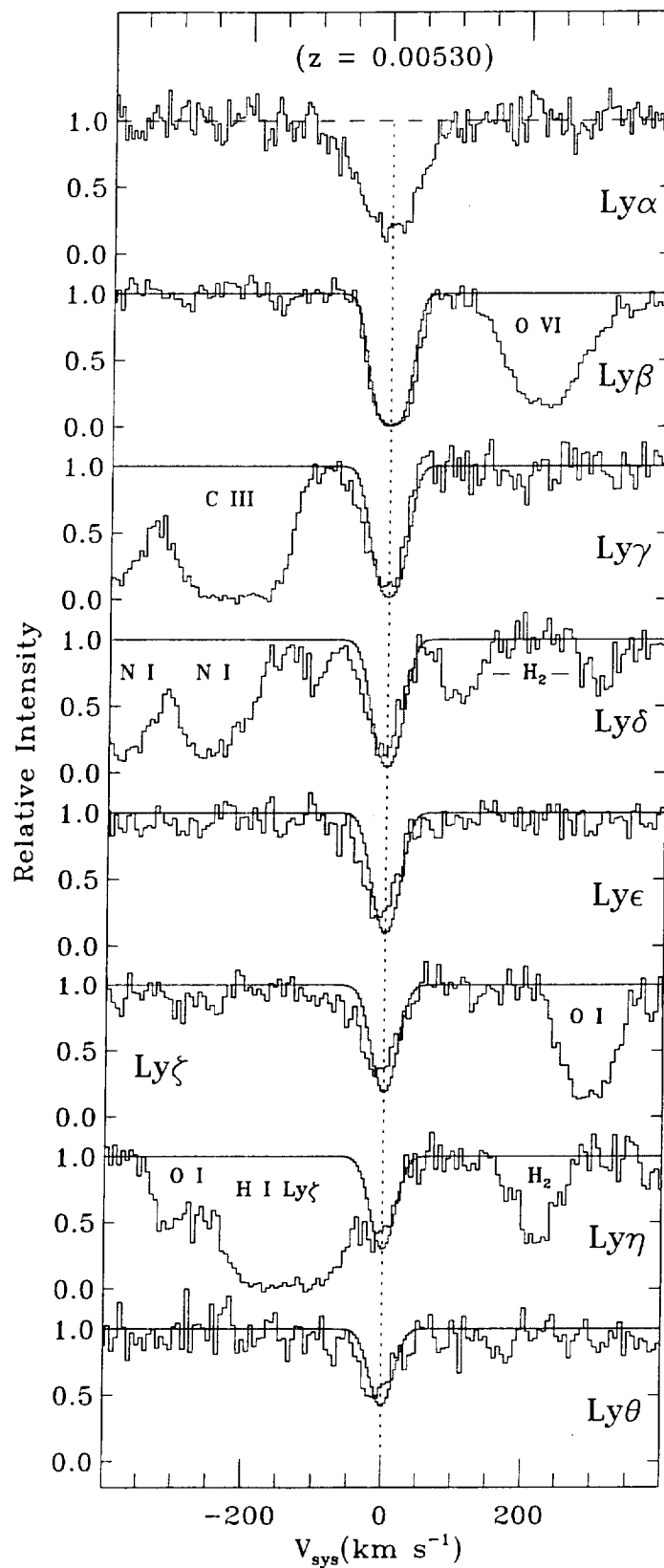
Fig. 4.— Caption on next page.

Fig. 4.–Continuum-normalized H I Lyman series absorption profiles for the $z = 0.00530$ (1590 km s^{-1}) Virgo absorber as observed by *FUSE*. The Lyα profile shown at the top of the plot is a pre-COSTAR GHRS spectrum. Note that the *FUSE* data are of higher resolution than the GHRS data since the GHRS data were obtained with an instrumental line spread function having very broad and strong (~ 40 km s^{-1}) wings. The Lyβ absorption in this system is very strong compared to the other absorbers along the sight line. The light grey lines overplotted on the spectra are the profiles constructed with the best fit single-component curve of growth parameters listed in Table 4 (see §4.1). These synthetic spectra have been convolved with a Gaussian instrumental function with $FWHM = 0.075$ Å. The actual line spread function may vary slightly with λ. Galactic lines are identified immediately above or below each spectrum.
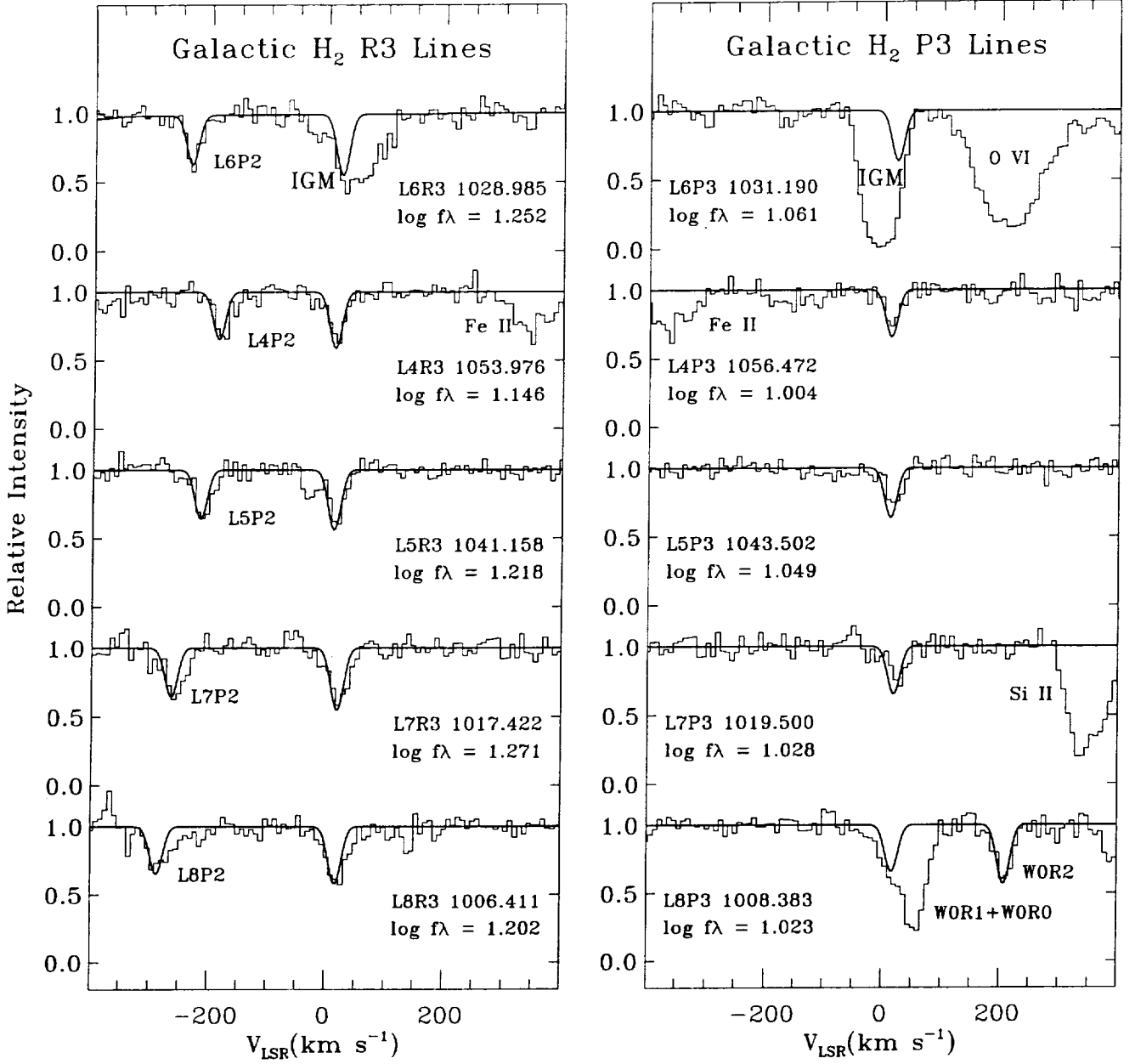
Fig. 5.— A comparison of the H_2 (6–0) R(3) and P(3) lines in the vicinity of the Virgo IGM absorbers with H_2 $J = 3$ lines of similar strength in other regions of the $FUSE$ spectra of 3C 273. The lines are plotted as a function of LSR velocity of the H_2 lines. For each line, the wavelength and product $\log f\lambda$ are listed. Additional H_2 and atomic lines covered in the plots are also labeled. The strong absorption features at the top of each panel are the $z = 0.00338$ Virgo absorber (left panel) and the $z = 0.00530$ Virgo absorber (right panel).
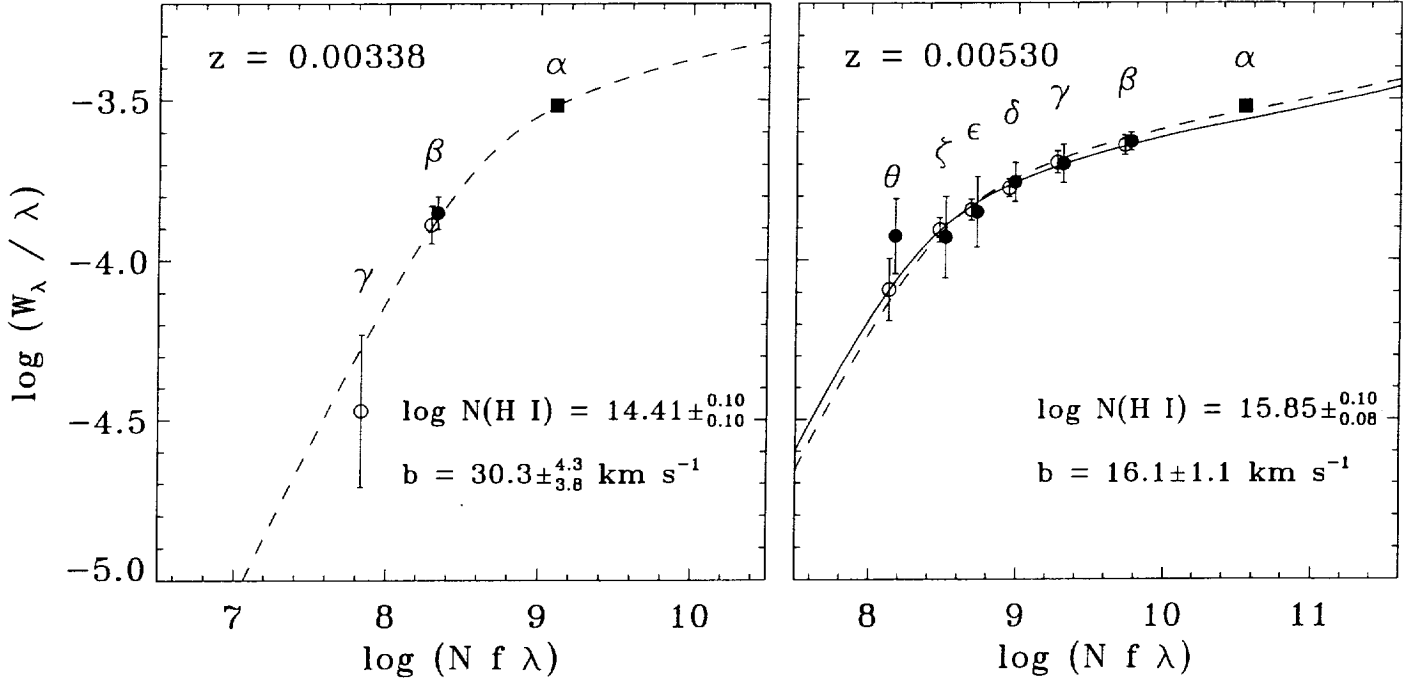
Fig. 6.— Single-component, Doppler-broadened curves of growth fitted to the H I lines observed in the $z = 0.00338$ (1015 km s^{-1}) and $z = 0.00530$ (1590 km s^{-1}) Virgo Cluster absorbers. The data points include GHRS data for Lyα (solid squares) and $FUSE$ data for H I lines on detectors 1 and 2 (filled and open circles, respectively). For the $z = 0.00338$ absorber, the fit shown includes the Lyα data point in the calculation. For the $z = 0.00530$ absorber, two fits are shown – one based solely on the $FUSE$ data (solid line), and one including the Lyα data (dashed line). The best fit column density for the $z = 0.00533$ absorber based on the $FUSE$ data is a factor of 43 higher than previous estimates based on Lyα profile fitting alone.
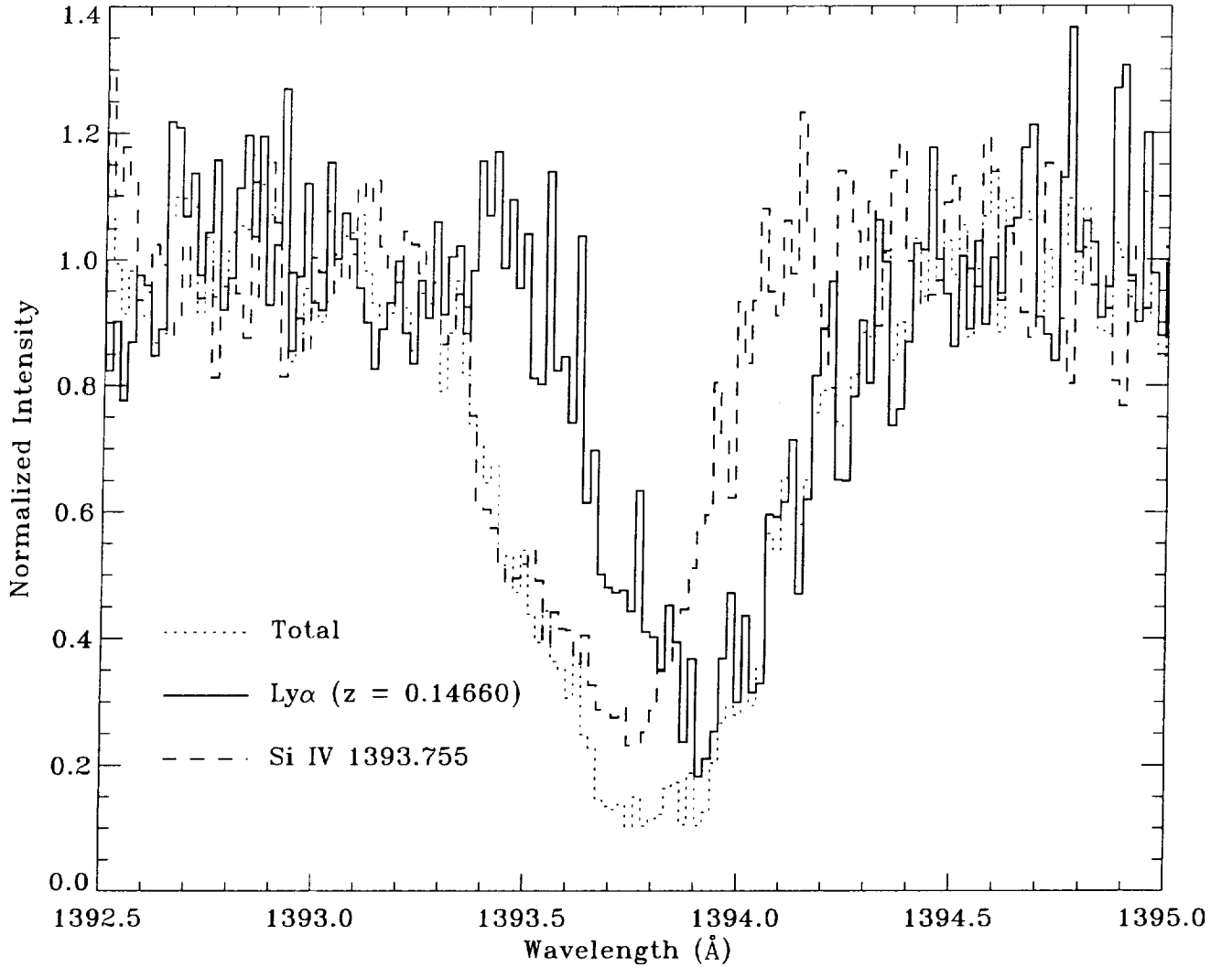
Fig. 7.— Decomposition of the $z = 0.14660$ Lyα absorber and the Galactic Si IV λ1393.755 line plotted as a function of LSR velocity. The dotted profile is the observed intergalactic Lyα plus interstellar Si IV λ1393.755 absorption. The solid and dashed lines show the decomposition into the IGM and ISM components. This decomposition differs from the one shown by Savage et al. (1993) - see §4.7 for details.
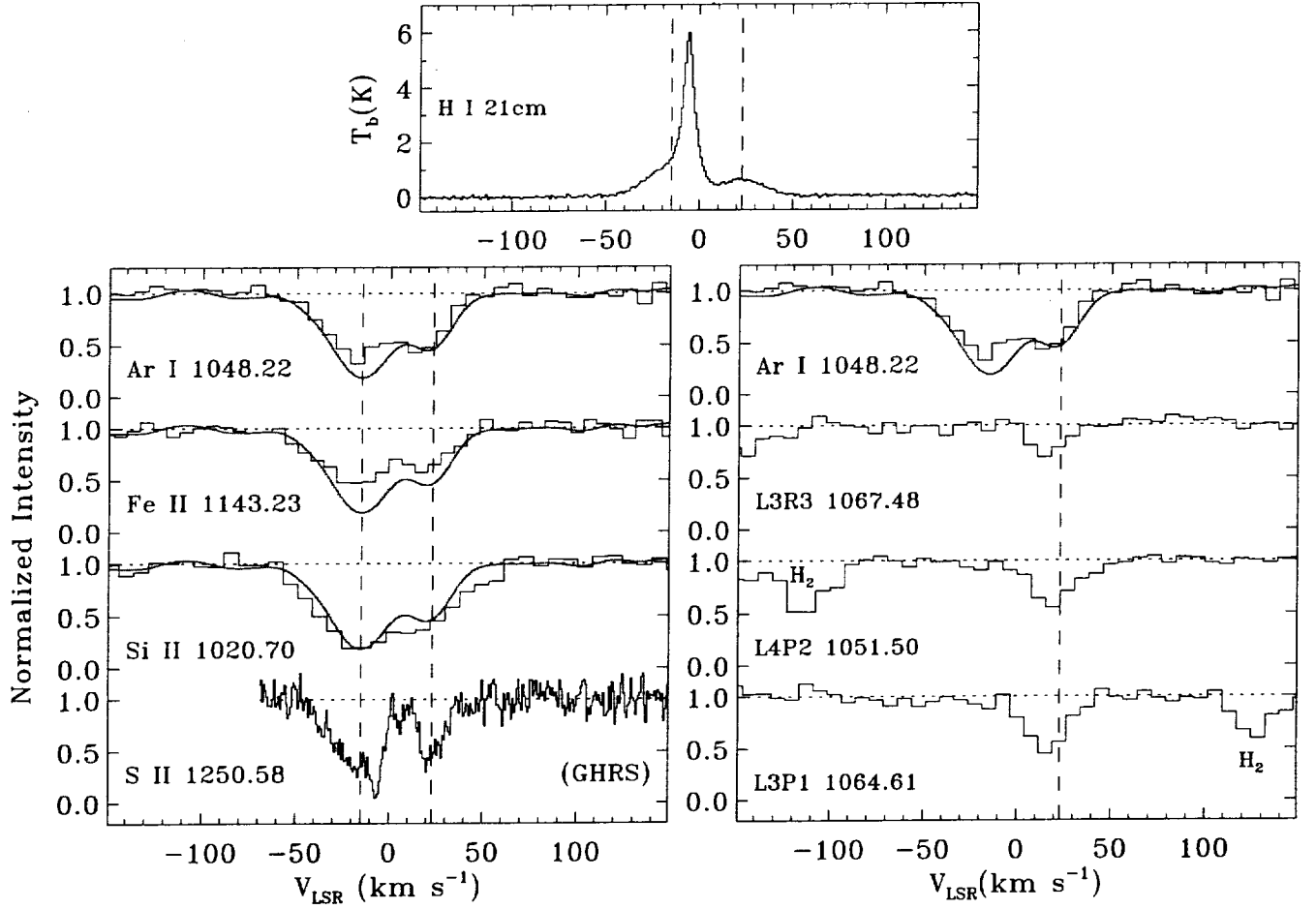
Fig. 8.— Low ion comparison for selected interstellar atomic and H_2 lines shown in Figures 1 and 2. The vertical dashed lines indicate the centroids of the negative and positive velocity groupings of clouds along the sight line. The light curve shown on top of the Ar I, Fe II, and S II profiles is the high-resolution (GHRS Ech-A) S II $\lambda1253.811$ line smoothed to a $FUSE$ resolution of ~ 20 km s^{-1}. Note that the H_2 absorption is closely aligned in velocity with the weaker of the two cloud groupings.
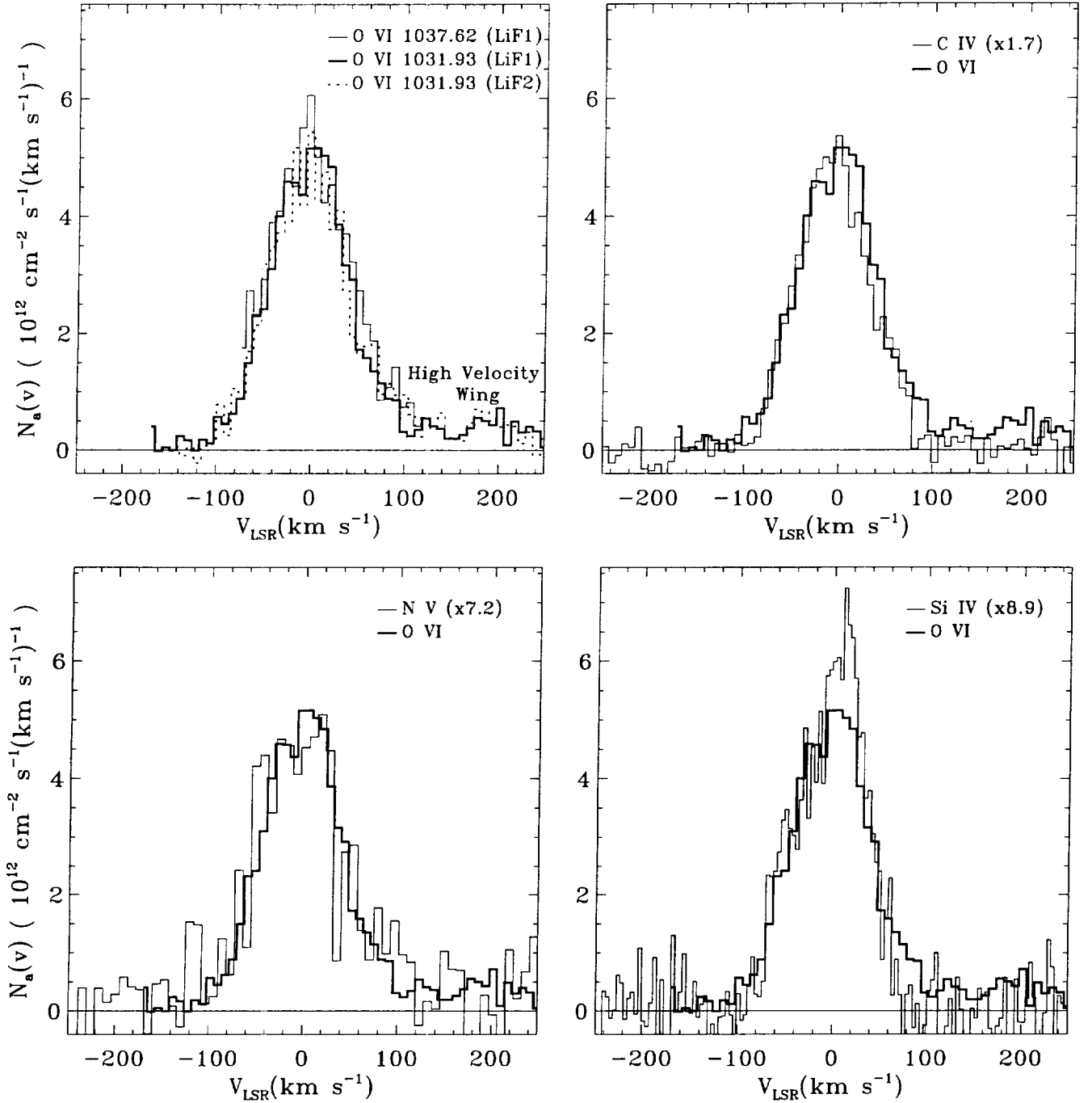
Fig. 9.— *Top left panel:* Apparent column density profiles versus LSR velocity for the interstellar O VI $\lambda\lambda 1031.926, 1037.617$ lines observed by *FUSE*. The two lines differ in the quantity $\log f\lambda$ by a factor of 2. The excellent agreement of the profiles indicates that there is no unresolved saturated structure within the line profiles. *Remaining panels:* Comparison of the O VI $\lambda 1031.926$ apparent column density profile with $N_a(v)$ profiles derived from GHRS data for C IV $\lambda 1550.770$ (*top right*), N V $\lambda 1238.821$ (*bottom left*), and Si IV $\lambda 1402.770$ (*bottom right*). The C IV, N V, and Si IV profiles have been scaled by factors equal to the values given in Eq. (5).
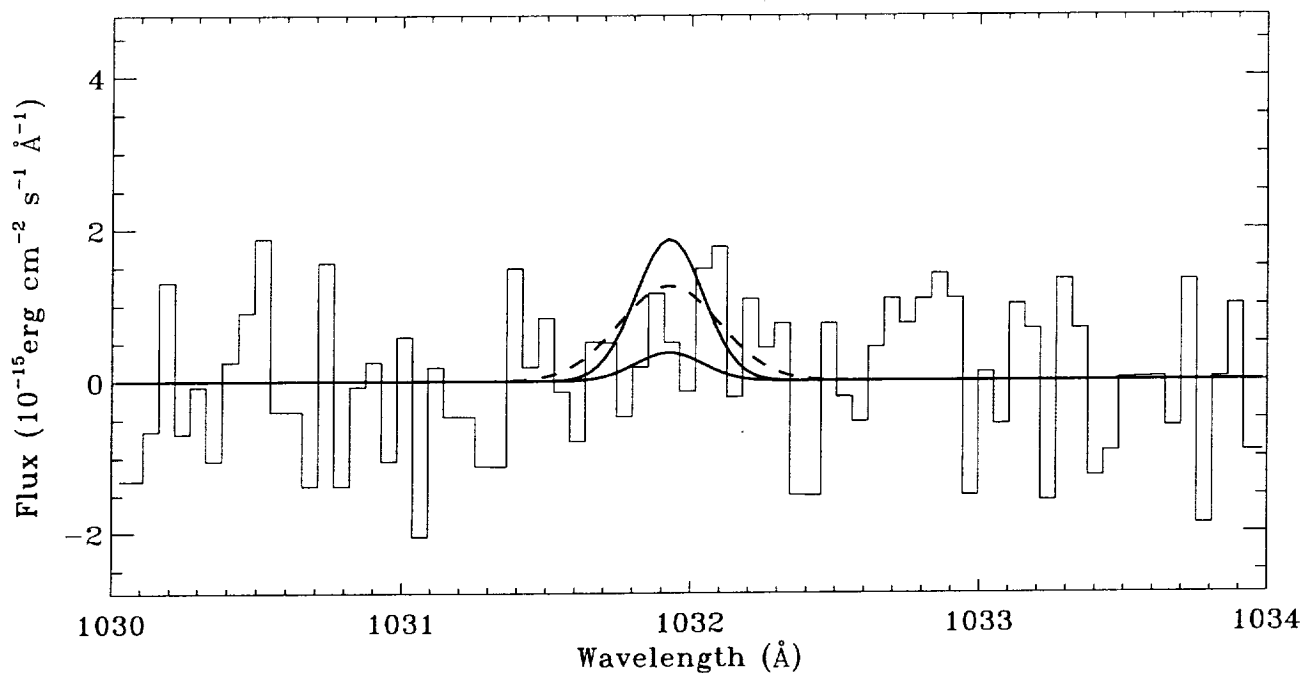
Fig. 10.— Extracted sky spectrum toward 3C 273 from the LiF1 MDRS aperture. The data (histogrammed line) have been binned into $\sim 0.06\,\text{Å}$ bins, and a constant "background" of 5×10^{-16} $\text{erg cm}^{-2}\,\text{s}^{-1}\,\text{Å}^{-1}$ has been subtracted from the nominally calibrated pipeline flux. The three smooth curves shown have the following parameters – solid lower profile: $I_{\lambda 1032} = 3000\ \text{ph cm}^{-2}\,\text{s}^{-1}\,\text{sr}^{-1}$, FWHM $= 80\ \text{km s}^{-1}$; solid upper profile: $I_{\lambda 1032} = 15{,}000\ \text{ph cm}^{-2}\,\text{s}^{-1}\,\text{sr}^{-1}$, FWHM $= 80\ \text{km s}^{-1}$; dashed profile: $I_{\lambda 1032} = 15{,}000\ \text{ph cm}^{-2}\,\text{s}^{-1}\,\text{sr}^{-1}$, FWHM $= 120\ \text{km s}^{-1}$.

Table 1.   Selected Interstellar Atomic Absorption Lines Toward 3C 273[a]

Species	λ (Å)	$\log f\lambda$	W_λ(Det1) (mÅ)	W_λ(Det2) (mÅ)	Vel. Range ($km\,s^{-1}$)	Note[b]
H I	1025.722	1.909	~ 1540	~ 1540	$\cdots$	1
C II	1036.337	2.106	474 ± 15	479 ± 17	-150 to $+40$	2
C III	977.020	2.872	533 ± 34	562 ± 13	-140 to $+100$	
N I	964.626	1.002	157 ± 24	157 ± 10	-80 to $+30$	
	1134.980	1.660	276 ± 10	259 ± 10	-100 to $+70$	
O I	1039.230	0.980	283 ± 10	314 ± 13	-100 to $+80$	
O VI	1037.617	1.836	> 240	> 240	$\cdots$	3
	1031.926	2.137	393 ± 15	392 ± 16	-160 to $+100$	4
			57 ± 10	57 ± 12	$+100$ to $+240$	34
Si II	1020.699	1.460	199 ± 10	203 ± 10	-100 to $+60$	
P II	1152.818	2.435	95 ± 10	97 ± 10	-100 to $+40$	
S II	1250.584	0.834	140 ± 07		-60 to $+40$	5
	1253.811	1.135	197 ± 05		-60 to $+40$	5
	1259.519	1.311	235 ± 14		-60 to $+40$	5
S III	1012.502	1.556	113 ± 10	111 ± 13	-65 to $+30$	6
S VI	944.523	2.314	45 ± 41	13 ± 13	-100 to $+100$	7
Ar I	1066.660	1.851	89 ± 10	76 ± 10	-120 to $+40$	
	1048.220	2.408	134 ± 10	145 ± 10	-90 to $+40$	

Table 1—Continued

Species	λ (Å)	$\log f\lambda$	W_λ(Det1) (mÅ)	W_λ(Det2) (mÅ)	Vel. Range ($\mathrm{km\,s^{-1}}$)	Note[b]
Fe II	1127.098	0.583	20 ± 10	25 ± 10	-100 to $+40$	
	1133.665	0.795	56 ± 10	54 ± 10	-100 to $+40$	
	1055.262	0.898	75 ± 10	69 ± 10	-100 to $+40$	
	1112.048	1.006	73 ± 10	50 ± 10	-100 to $+40$	8
	1125.448	1.255	137 ± 10	148 ± 10	-120 to $+60$	9
	1143.226	1.308	131 ± 10	144 ± 10	-100 to $+40$	
	1121.975	1.329	165 ± 10	154 ± 10	-100 to $+40$	
	1096.877	1.545	$\cdots$	201 ± 10	-100 to $+40$	10
	1144.938	2.084	302 ± 10	297 ± 10	-100 to $+40$	
Fe III	1122.526	1.947	160 ± 10	172 ± 10	-100 to $+50$	

[a]Wavelengths and f-values are from Morton (1991). Errors are 1σ estimates and limits are 3σ estimates unless otherwise indicated.

[b]Notes: (1) Equivalent widths derived from a fit to the damping wings of the Lyβ line, for which $\log N(\mathrm{H\ I}) = 20.20$. (2) H_2 Lyman (5–0) R(0) occurs at $+60$ $\mathrm{km\,s^{-1}}$ with respect to C II. (3) Equivalent width is quoted as a limit for comparison with $\lambda 1031.926$ since it was derived over the limited velocity range of -90 to $+60$ $\mathrm{km\,s^{-1}}$. (4) Total O VI $\lambda 1031.926$ equivalent width (-160 to $+240$ $\mathrm{km\,s^{-1}}$) is 450 ± 15 mÅ. (5) S II values from HST data. The $\lambda 1250.584$ and $\lambda 1253.811$ are from post-COSTAR GHRS Ech-A data, and the $\lambda 1259.519$ value is from pre-COSTAR GHRS G160M data. (6) H_2 Werner (0–0) P(2) at 1012.17 Å (-99 $\mathrm{km\,s^{-1}}$ w.r.t. S III), W0Q3 at 1012.68 Å, and L7R0 at 1012.81 Å bracket the S III line. (7) Stronger S VI line at 933.378 Å is blended with H_2 L16R2 and W4Q3 lines. (8) Line appears as a much broader feature in the LiF1B spectrum. The equivalent widths of this feature are uncertain since the feature should be at least as strong as the $\lambda 1055.262$ line. (9) Feature centered at -122 $\mathrm{km\,s^{-1}}$ with $W_\lambda \approx 15$ mÅ appears in both channels and is of unknown origin. It is not likely to be Fe II because it is not present in the stronger Fe II lines. (10) Line falls near edge of segment LiF1B, leading to an unreliable value of W_λ on detector 1.

Table 2. Selected Interstellar H_2 Absorption Lines Toward 3C 273

Transition[a]	λ (Å)	$\log f\lambda$	$W_\lambda(\text{Det1})$[b] (mÅ)	$W_\lambda(\text{Det2})$[b] (mÅ)	$\log N$ (3σ)
		$J = 3$			
L3R3	1067.480	1.033	21±5	37±9	⋯
L4R3	1053.980	1.146	45±5	42±9	⋯
L5R3	1041.160	1.218	57±6	< 74[c]	⋯
L7R3	1017.420	1.271	56±6	44±8	⋯
L7P3	1019.500	1.028	35±7	33±8	⋯
L8R3	1006.410	1.202	64±15	55±13	⋯
W0R3	1010.130	1.143	36±7	33±8	⋯
L0P3	1099.790	0.432	12±6	14±5	⋯
L3P3	1070.140	0.903	32±6	36±7	⋯
L4P3	1056.470	1.004	30±5	44±10	⋯
W2P3	970.560	0.978	⋯	31±9	⋯
W3Q3	950.400	1.411	⋯	50±10	⋯
		$J = 4$			
L3R4	1070.900	1.015	6±10	12±12	<14.49
L4R4	1057.380	1.135	16±10	14±10	<14.37
L5P4	1047.550	1.062	3±10	−5±12	<14.44
L5R4	1044.540	1.206	3±10	−2±12	<14.31
W0R4	1011.810	1.147	8±10	8±12	<14.38
L9R4	999.270	1.221	8±13	0±16	<14.42
W1P4	994.230	1.138	−8±15	26±17	<14.57

[a]Notation for the H_2 lines is as follows: "L" indicates Lyman series transitions. "W" indicates Werner series transitions. The first numerical digit indicates the upper vibrational state of the transition (the lower vibrational state is 0 in all cases). The last two characters indicate the rotational transition selection rule (P, Q, R) and the upper rotational level (3 or 4).

[b]Errors are 1σ estimates.

[c]Absorption is broader and stronger than expected. Possible fixed-pattern noise contamination.

Table 3. Intergalactic Absorption Lines Toward 3C 273[a]

Species	λ_{rest} (Å)	λ_{obs} (Å)	$W_{obs}(\#1)$[b] (mÅ)	$W_{obs}(\#2)$[b] (mÅ)	Comments[c]
			$z = 0.00338$		
Lyα	1215.670	1219.743	371±17		GHRS G160M pre-COSTAR data
Lyβ	1025.722	1029.158	170±16	158±17	H_2 L6R3 contribution to listed W_{obs} is ≈ 25 mÅ
Lyγ	972.537	975.795	0±33	33±14	
O VI	1031.926	1035.383	26±10	25±10	H_2 L6P4 nearby expected to be weak
	1037.617	1041.093	<30	<30	Blended with H_2 L5R3
C III	977.020	980.293	18±40	9±10	
			$z = 0.00530$		
Lyα	1215.670	1222.150	367±13		GHRS G160M pre-COSTAR data
Lyβ	1025.722	1031.189	257±10	251±11	H_2 L6P3 contribution to listed W_{obs} is ≈ 16 mÅ
Lyγ	972.537	977.721	195±25	197±15	
Lyδ	949.743	954.805	167±22	160±10	
Lyε	937.804	942.802	133±30	135±10	H_2 L15R3 nearby but does not interfere
Lyζ	930.748	935.709	121±28	127±10	H_2 L16R3 contribution to listed W_{obs} is ≈ 11 mÅ
Lyη	926.226	931.163	⋯	⋯	In positive velocity wing of Galactic H I Lyζ
Lyθ	923.150	928.070	110±26	85±13	
O VI	1031.926	1037.426	⋯	⋯	Blended with C II* λ1037.012 and H_2 L5R1
	1037.617	1043.147	17±10	5±11	
C III	977.020	982.227	⋯	< 74	Blended with H_2 L10R1

Table 3—Continued

Species	λ_{rest} (Å)	λ_{obs} (Å)	$W_{obs}(\#1)^b$ (mÅ)	$W_{obs}(\#2)^b$ (mÅ)	Comments[c]
				$z = 0.02947$	
Lyα	1215.670	1251.496	139±07		GHRS Ech-A post-COSTAR data
			129±14		GHRS G160M pre-COSTAR data
Lyβ	1025.722	1055.950	29±10	15±10	
O VI	1031.926	1062.337	−5±10	5±10	
	1037.617	1068.195	0±10	2±11	
C III	977.020	1005.813	10±10	3±10	H$_2$ L8P2 nearby but does not interfere
				$z = 0.04898$	
Lyα	1215.670	1275.201	126±14		GHRS G160M pre-COSTAR data
Lyβ	1025.722	1075.952	23±10	−2±22	SiC2B
O VI	1031.926	1082.459	46±43	−6±26	SiC1A, SiC2B
	1037.617	1088.429	−8±46	−3±24	SiC1A, SiC2B
C III	977.020	1024.865	⋯	⋯	Line falls in wing of Galactic Lyβ
				$z = 0.06655$	
Lyα	1215.670	1296.573	312±13		GHRS G160M pre-COSTAR data
Lyβ	1025.722	1093.984	⋯	125 ± 10	Line falls in detector #1 wavelength gap
					H$_2$ L1P1 contribution to listed W_{obs} is ≈ 25 mÅ
					C III at $z = 0.12007$ is nearby
Lyγ	972.537	1037.259	⋯	⋯	Blended with Galactic C II/C II*/H$_2$ absorption
O VI	1031.926	1100.601	3±10	6±10	
	1037.617	1106.670	0±10	−7±12	
C III	977.020	1042.041	10±10	21±15	

Table 3—Continued

Species	λ_{rest} (Å)	λ_{obs} (Å)	$W_{obs}(\#1)^{b}$ (mÅ)	$W_{obs}(\#2)^{b}$ (mÅ)	Comments[c]
			$z = 0.09012$		
Lyα	1215.670	1325.226	160±20		GHRS G160M pre-COSTAR data, very broad line
Lyβ	1025.722	1118.160	34±10	27±13	Line very weak, subject to continuum placement
O VI	1031.926	1124.923	<45	<39	Blended with Fe II λ1133.665
	1037.617	1131.127	17±10	12±10	Subject to continuum placement
C III	977.020	1065.069	<25	<30	No line present after removing H$_2$ L3R2
			$z = 0.12007$		
Lyα	1215.670	1361.635	138±11		GHRS G160M pre-COSTAR data
Lyβ	1025.722	1148.880	31±10	28±10	
Lyγ	972.537	1089.309	0±42	–3±13	SiC1A, not covered by LiF1A
O VI	1031.926	1155.829	33±11	27±10	
	1037.617	1162.204	18±10	17±10	
C III	977.020	1094.331	$\cdots$	32±10	Line falls in detector #1 wavelength gap H$_2$ L1R2 (ISM) and Lyβ ($z = 0.06655$) nearby
			$z = 0.14660$		
Lyα	1215.670	1393.887	355±20		GHRS G160M pre-COSTAR data (deblended)[d]
Lyβ	1025.722	1176.093	67±13	78±16	
Lyγ	972.537	1115.111	15±10	5±11	
O VI	1031.926	1183.206	14±12	$\cdots$	Outside *FUSE* detector #2 bandpass
	1037.617	1189.732	$\cdots$	$\cdots$	Outside *FUSE* bandpass
C III	977.020	1120.251	2±13	5±11	

[a]Errors are 1σ estimates and limits are 3σ estimates unless otherwise indicated.

[b]Equivalent widths measured on *FUSE* detectors 1 and 2. Unless otherwise specified in the comments, values refer to LiF1/LiF2 for $\lambda > 990$ Å, and SiC1/SiC2 for $\lambda < 990$ Å.

[c]Notation for molecular hydrogen (H$_2$) lines is the same as specified for Table 2 - see note a of that table.

[d]Value for deblended profile shown in Figure 7.

Table 4. Intergalactic Medium Column Densities[a]

z	v_{helio} ($\mathrm{km\,s^{-1}}$)	b(H I) ($\mathrm{km\,s^{-1}}$)	$\log N$(H I) ($\mathrm{cm^{-2}}$)	$\log N$(O VI) ($\mathrm{cm^{-2}}$)	$\log N$(C III) ($\mathrm{cm^{-2}}$)	$\frac{N(HI)}{N(OVI)}$	Note[b]
0.00338	1015	$30.3\pm^{4.3}_{3.8}$	$14.41\pm^{0.10}_{0.10}$	$13.32\pm^{0.13}_{0.21}$	<12.67	12.3 ± 5.7	1,3
0.00530	1590	16.1 ± 1.1	$15.85\pm^{0.10}_{0.08}$	<13.68	<13.08	>148	2
		17.5 ± 1.5	$15.77\pm^{0.12}_{0.10}$	$\cdots$	$\cdots$	>123	1
0.02947	8840	$23.8\pm^{22.2}_{9.4}$	$13.55\pm^{0.17}_{0.12}$	<13.38	<12.67	>1.5	1,4
0.04898	14695	$20.9\pm^{23.1}_{9.8}$	$13.50\pm^{0.25}_{0.14}$	<13.79	$\cdots$	>0.5	1,4
0.06655	19965	$25.9\pm^{3.2}_{2.5}$	$14.21\pm^{0.11}_{0.09}$	<13.38	<12.71	>6.8	1
0.09012	27035	$21.2\pm^{\cdot}_{7.4}$	$13.64\pm^{0.14}_{0.14}$	<13.49	<12.59	>1.4	1
0.12007	36020	$15.5\pm^{16.3}_{4.2}$	$13.61\pm^{0.16}_{0.15}$	$13.38\pm^{0.18}_{0.12}$	$12.45\pm^{0.19}_{0.36}$	$1.7\pm^{0.6}_{0.8}$	1,5,6
0.14660	43980	$46.1\pm^{27.3}_{10.1}$	$13.95\pm^{0.08}_{0.08}$	<13.46	<12.71	>3.1	1

[a]Errors are 1σ estimates unless specified otherwise. Limits are 3σ estimates based upon the measured equivalent widths and the assumption of a linear curve of growth.

[b]Notes: (1) H I curve-of-growth results include Lyα. (2) H I curve-of-growth results exclude Lyα. (3) O VI result based on linear curve of growth. Broad weak O VI $\lambda1031.926$ absorption is present in both LiF1A and LiF2B. The 1σ error on N(O VI) was derived from single channel values of the equivalent width. Combination of data from both channels implies a significance of $3-4\sigma$. (4) Upper limit on b(H I) set by observed width of profile. (5) O VI result based on curve of growth; best fitting b-value is 7.2 $\mathrm{km\,s^{-1}}$, but higher values are allowed. Errors span the column density range expected for b-values of 3–50 $\mathrm{km\,s^{-1}}$. (6) C III column density limit assuming equivalent width limit of 30 m$\mathrm{\AA}$.

Table 5.   Interstellar Medium Column Densities[a]

Species	$\log N$ (Negative)	$\log N$ (Positive)	$\log N$ (Total)	Method[b]	Note[c]
H I	20.15	19.45	20.23	$\cdots$	1
	$\cdots$	$\cdots$	20.20 ± 0.05	PF	2
$H_2(J = 0)$	$\cdots$	$\cdots$	15.00 ± 0.30	PF	3
$H_2(J = 1)$	$\cdots$	$\cdots$	15.48 ± 0.18	PF	3
$H_2(J = 2)$	$\cdots$	$\cdots$	14.76 ± 0.12	COG, PF	3
$H_2(J = 3)$	$\cdots$	$\cdots$	14.73 ± 0.12	COG, PF	3
$H_2(J = 4)$	$\cdots$	$\cdots$	< 14.40	AOD	
O VI	$\cdots$	$\cdots$	14.73 ± 0.04	AOD	4
			14.77 ± 0.05	AOD	5
Si II	~ 14.90	~ 14.68	15.10 ± 0.10	AOD, COG	6
P II	~ 13.55	~ 12.84	13.60 ± 0.04	AOD	
P III	< 13.70	< 13.40	< 13.88	AOD	
S II	~ 15.33	~ 14.88	15.46 ± 0.06	AOD, COG	7
S III	$\cdots$	$\cdots$	14.64 ± 0.06	AOD	
S VI	$\cdots$	$\cdots$	< 13.36	AOD	
Ar I	~ 14.32	~ 13.65	$14.40\pm^{0.19}_{0.13}$	AOD, COG	8

Table 5—Continued

Species	$\log N$ (Negative)	$\log N$ (Positive)	$\log N$ (Total)	Method[b]	Note[c]
Fe II	~ 14.89	~ 14.40	15.01 ± 0.08	AOD, COG	9
Fe III	~ 14.23	~ 13.77	14.36 ± 0.04	AOD	

[a]Errors are 1σ estimates unless specified otherwise. Limits are 3σ estimates based upon either the apparent optical depth limits or the measured equivalent widths and the assumption of a linear curve of growth.

[b](COG): Curve of growth fit to the measured equivalent widths of the lines for each species. The derived Doppler parameters listed in the notes below are measures of the overall extent of profiles, not of the individual component widths. (PF): Profile fitting for the H_2 lines. The synthetic H_2 spectrum was constucted as indicated in the text. (AOD): Apparent optical depth method. Column densities are direct integrations of the apparent column density profiles constructed for each species.

[c]Notes:

(1) H I: Column densities derived from integration of the NRAO 21 cm profile measured by Murphy, Sembach, & Lockman (unpublished). The emission was assumed to be optically thin.

(2) H I: Column density derived from a profile fit to the radiation damping wings of the Lyβ line at 1025.7 Å.

(3) These H_2 values are appropriate for a Doppler parameter $b \approx 6 \pm 2$ km s^{-1}. The absorption is centered near $\sim +23$ km s^{-1}.

(4) O VI: Velocity range of integration is -160 km s^{-1} to $+100$ km s^{-1}.

(5) O VI: Velocity range of integration is -160 km s^{-1} to $+240$ km s^{-1}.

(6) Si II: $b_{COG} = 32.2 \pm 2.5$ km s^{-1}. Lines used include $\lambda\lambda 1020.699$, 1260.433 (HST), 1304.370 (HST), and 1526.707 (HST).

(7) S II: $b_{COG} = 20.1 \pm 2.5$ km s^{-1}. Lines used include $\lambda\lambda 1250.584$ (HST), 1253.811 (HST), 1259.519 (HST).

(8) Ar I: $b_{COG} = 12.1 \pm 2.0$ km s^{-1}. Lines used include $\lambda\lambda 1048.220$, 10660.660.

(9) Fe II: $b_{COG} = 28.0 \pm 2.5$ km s^{-1}. Lines used include $\lambda\lambda 1055.262$, 1096.877, 1112.048, 1121.975, 1125.448, 1133.665, 1143.226, 1144.938, 2586.650 (HST), and 2600.173 (HST).

Table 6.   Ion Ratios and Elemental Abundances[a]

Ratios	
$N(P\ \text{III})/N(P\ \text{II}+P\ \text{III})$	< 1.90
$N(S\ \text{III})/N(S\ \text{II}+S\ \text{III})$	0.13 ± 0.02
$N(Fe\ \text{III})/N(Fe\ \text{II}+Fe\ \text{III})$	0.18 ± 0.04
Abundances[b]	
$(S/H) = N(S\ \text{II})/N(H\ \text{I})$	$0.91 \pm 0.12\ (S/H)_\odot$
$(Ar/S) = N(Ar\ \text{I})/N(S\ \text{II})$	$0.45 \pm 0.13\ (Ar/S)_\odot$
$(Si/S) = N(Si\ \text{II}+Si\ \text{III})/N(S\ \text{II}+S\ \text{III})$	$\geq 0.20\ (Si/S)_\odot$
$(P/S) = N(P\ \text{II}+P\ \text{III})/N(S\ \text{II}+S\ \text{III})$	$0.6 - 1.7\ (P/S)_\odot$
$(Fe/S) = N(Fe\ \text{II}+Fe\ \text{III})/N(S\ \text{II}+S\ \text{III})$	$0.22 \pm 0.04\ (Fe/S)_\odot$

[a]Errors are 1σ estimates. Limits are 3σ estimates.

[b]Solar system reference abundances are from Anders & Grevesse (1989) on a logarithmic abundance scale where $A(H)$ = 12.00, $A(Si)$ = 7.55, $A(P)$ = 5.57, $A(S)$ = 7.27, $A(Ar)$ = 6.56, and $A(Fe)$ = 7.51.

Table 7. Galactic Halo Column Density Ratios

Sight Line	$l(°)$	$b(°)$	$\dfrac{N(O\,VI)}{N(N\,V)}$	$\dfrac{N(O\,VI)}{N(C\,IV)}$	$\dfrac{N(O\,VI)}{N(Si\,IV)}$	Notes[a]
3C 273	289.95	+64.36	7.2 ± 1.1	1.7 ± 0.2	8.9 ± 1.1	1
ESO 141-55	338.18	−26.71	4.8 ± 1.1	0.6 ± 0.2	3.5 ± 0.6	2
PKS 2155-304	17.73	−52.25	3.9 ± 1.1	1.6 ± 0.2	⋯	
Mrk 509	35.97	−29.86	6.8 ± 1.2	1.8 ± 0.2	5.1 ± 1.0	3
H 1821+643	94.00	+27.42	2.6 ± 0.5	1.6 ± 0.3	⋯	4

[a]All errors are 1σ estimates. Values of N(O VI) are from Savage et al. (2000), and values of N(C IV) and N(N V) are from Savage et al. (1997) unless specified otherwise as follows: (1) Values are from this work and do not include O VI associated with the positive velocity wing. Including the positive velocity O VI wing increases the ratios by 10%. (2) Sembach et al. (1999a). A substantial saturation correction was required for N(C IV); (3) Values do not include the highly ionized high velocity clouds detected by Sembach et al. (1999b) and Sembach et al. (2000b). N(Si IV) was measured from data obtained by Sembach et al. (1999b); (4) N(O VI) is from Oegerle et al. (2000).